Chapter 2: Ti_3C_2/Co_3O_4 nanocomposite as anode catalyst for methanol oxidation

2.1 Introduction

In energy conversion [1, 2] and storage devices [3, 4], transition metal oxides (TMOs) have attracted attention because of their superior electrochemical characteristics, cost effectiveness, controllable chemical and textural properties. The remarkable electrochemical capabilities of TMOs, resulting from the existence of numerous oxidation states of metal cations, and their excellent stability in alkaline media make them a viable substitute for the noble metal-based electrocatalysts. Moreover, their Lewis acid-base properties make them suitable for electrocatalytic applications [5]. Since TMOs are more stable in alkaline media, a variety of TMOs, such as NiO, $Ni(OH)_2$, Co_3O_4, and MnO_x, etc., are frequently utilized as anode catalysts in alkaline DMFCs [2, 5]. In alkaline medium, different oxidation states of Co are observed, viz. CoO (+2), Co_2O_3 (+3), CoO_2 (+4), and Co_3O_4 (+2, +3). Co (II) and Co (III) ions occupy the tetrahedral and octahedral sites, respectively, in the spinel structure of Co_3O_4 with the mixed valence state [6]. Recently, spinel Co_3O_4 is emerging as a versatile material in various applications of energy storage and conversion due to its enriched redox chemistry, less toxicity, good reversibility, high thermal and mechanical stability, and high electrocatalytic ability [7, 8, 9]. Co_3O_4 is hybridized with a variety of carbon-based supports, including carbon nanofibers, graphene, porous carbon, carbon nanotubes, and reduced graphene oxide, to compensate its poor conductivity and surface area [10-12]. Heterogeneous mesoarchitecture of N-Co_3O_4@C-NRPs (NRPs representing nanorod pellets NRPs), exhibits superior methanol oxidation reaction (MOR) activity and long-term stability than Pt/C due to the Co^{3+} sites present along the crystal {112} facet [13]. In the recent times, 2D layered materials of transition metal carbide/nitride or carbonitride (MXenes) are attracting attention in energy conversion and storage devices. Given its unique combination of metallic conductivity, surface hydrophilicity, and excellent mechanical characteristics, MXene might be envisioned as a potential support material in this context [14, 15]. MXenes ($M_{n+1}X_nT_x$ with n = 1, 2, 3) are produced by selectively etching the 'A' layer from the MAX phase, where X can be either carbon or nitrogen, A can be an element of the IIIA or IVA group, and M is an early transition metal element [15] and T_x represents surface terminating functional groups like OH, O

and F [16]. MXene is becoming a versatile material with a wide range of applications due to its fascinating features, particularly in electrochemical energy storage [19], electrical devices [17], catalysis [18], and energy conversion devices [5]. MXenes have been investigated as a competitive catalyst support for noble metal nanoparticles, such as Pt, Pd, Ru, etc. [5], as well as their alloys [5, 20], and other non-Pt catalysts [21] in the research of various fuel cells. As obtaining stable and CO resistant non-noble metal electrocatalysts is currently of more interest, MXene can be explored as a support material for electroactive materials beyond the Pt-group metals. Since MXenes and TMOs have Lewis acid-base sites, MXene/TMO nanocomposite presents itself as a promising alternative electrocatalyst in alkaline DMFC.

This chapter focuses on the development of hybrid nanosystem, $Ti_3C_2T_x/Co_3O_4$ as a DMFC anode catalyst in alkaline medium. Non-noble metal oxide Co_3O_4 is hybridized with MXene to yield MOR current density comparable to that of Pt group-based anode catalysts. Faster MOR kinetics are obtained by a significant interaction between the Lewis basic hydroxyl groups on the surface of MXene and the distinct Lewis acid nature of spinel Co_3O_4. Adding MXene nanosheets to Co_3O_4 nanoparticles reduces their agglomeration and increases the number of exposed active sites. MXene as support material provides larger surface area for methanol adsorption, further reducing the charge transfer resistance. Thus, the nanocomposite presents a viable substitute for the expensive Pt-based anode catalyst due to the synergistic contributions of both components.

2.2 Experimental section

2.2.1 Material synthesis

2.2.1.1 Synthesis of MXene $Ti_3C_2NH_4T_x$: A finite (0.5 g) amount of MAX (Ti_3AlC_2) was added slowly to 30 ml of 2M NH_4HF_2 (etchant) and the reaction was run for 24 hours at room temperature. The reaction product was washed with distilled water and ethanol until the pH becomes neutral. The resulting slurry was dried in a drying oven for 12 hours at 80° C. To increase the interlayer spacing and delaminate the prepared MXene, 0.2 g $Ti_3C_2NH_4T_x$ was added to 30 ml of intercalant dimethyl sulfoxide (DMSO) followed by stirring for 24 hours. The MXene nanosheets were obtained thereafter by disseminating the DMSO intercalated $Ti_3C_2NH_4T_x$ in distilled water and sonicating for few hours in a nitrogen environment to prevent oxidation of the MXene nanosheets.

2.2.1.2 Synthesis of Co_3O_4: Co_3O_4 was prepared by annealing a finite amount (1 g) of Co precursor, $Co(NO_3)_2 \cdot 6H_2O$ at 420°C in a muffle furnace for 3 hours.

2.2.1.3 Synthesis of Ti_3C_2/Co_3O_4 (TC): Ti_3C_2/Co_3O_4 was synthesized by a simple hydrothermal process. Cobalt nitrate hexahydrate (0.6 g) and urea (0.6185) were added slowly into 70 ml of 25 M NaOH solution, maintaining stoichiometric ratio of 1:5. The mixture is then stirred until a homogeneous dark blue solution is obtained. Afterward, a finite amount of $Ti_3C_2NH_4T_x$ (0.03 g) was added into the solution and left to stir in absence of oxygen. After achieving a homogeneous solution, the suspension was transferred to a Teflon lined autoclave after expelling the air with nitrogen gas. The autoclave was then heated in a drying oven at 120 °C for a day. After the hydrothermal treatment, black powder was obtained by centrifugation and vigorous washing process, followed by drying in an oven at 40 °C for a day. The dry black powder was then annealed in air at 280 °C for 3 hr to obtain the hybrid nanocomposite Ti_3C_2/Co_3O_4. The schematic of the synthesis method is displayed in fig. 2.1

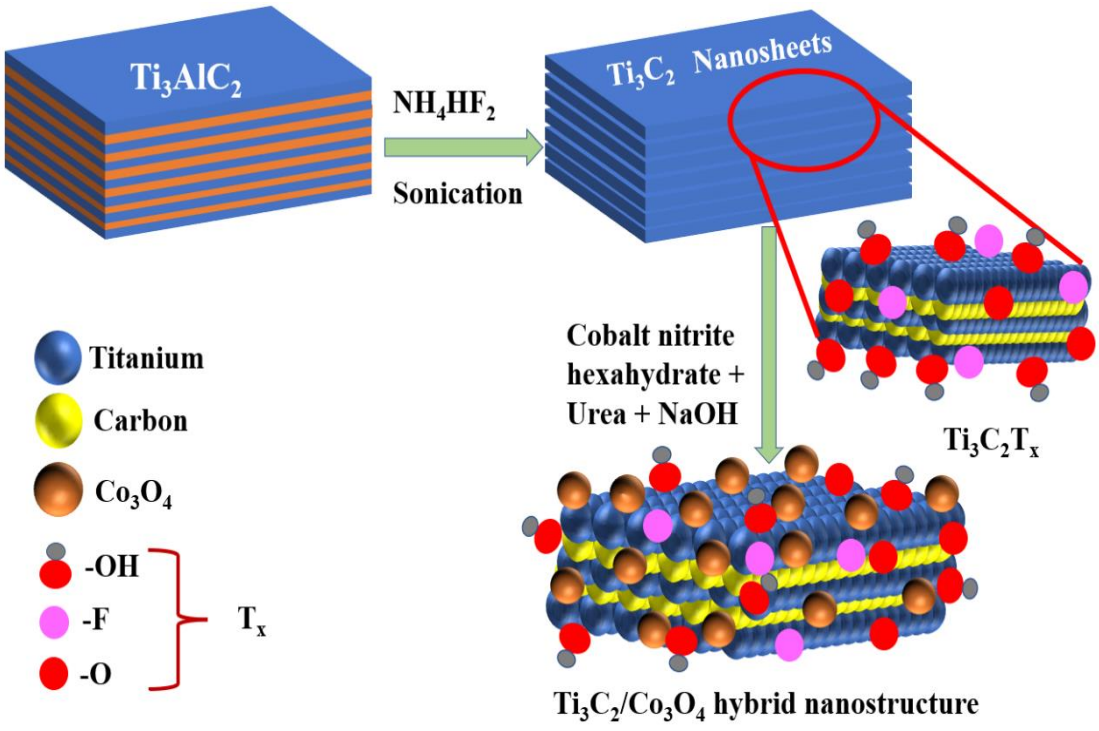

Figure 2.1: Synthesis route of the nanocomposite Ti_3C_2/Co_3O_4

2.2.2 Material characterizations:

X-ray diffraction (Bruker Axs, Germany model D8 Focus), Fourier transform infrared spectroscopy (PerkinElmer spectrometer of model Frontier MIR FIR) and X-ray photoelectron spectroscopy (Thermo Fisher Scientific Pvt. Ltd., UK Model ESCALAB Xi+) were done to study the crystalline and chemical structures of the samples. The morphology of the samples was visualized using Field emission scanning electron microscopy (FESEM) (JSM-7200F) and Transmission Electron Microscopy (TEM) (TECNAI G2 20 S-TWIN (200KV)). The elemental composition of the prepared samples was evaluated using energy-dispersive X-Ray spectrometer JEOL, JAPAN of make JSM 6390LV. The specific surface area and pore size distribution was studied by Brunauer-Emmett-Teller measurements (Quantachrome, Nova 1000E).

2.2.3 Electrochemical characterizations:

All the electrochemical measurements were conducted by Autolab 302N Modular potentiostat galvanostat, FRA 32M Module, Netherlands in 3 electrode system at room temperature. The system consisted of Pt wire as the counter electrode, Ag/AgCl as the reference electrode and glassy carbon (5 mm) electrode (GCE) coated with prepared catalysts as the working electrode. The GCEs were washed first by distilled water and then gently polished with alumina suspension (0.05 µm alumina) on velvet pads. Finally, after washing with distilled water, they were kept in air to dry. The working electrodes were developed by preparing a catalyst ink consisting of prepared samples, carbon black and nafion (maintaining mass ratio of 75:15:10) dispersed into a solution of ethanol and water. Equal drops of the above solution were casted on the GCE and left to dry at room temperature. The electrochemical characterizations were carried out in alkaline medium using 0.5M NaOH as the supporting electrolyte. The electrocatalytic activity of the prepared electrodes were investigated by cyclic voltammetry (CV), chronoamperometry (CA), and electrochemical impedance spectroscopy (EIS) in 0.5M NaOH solution by varying the concentration of methanol. All the CVs were performed in the potential range (-0.3 to +0.65) V by varying the scan rates. CA measurements were carried out at 0.65 V for 1 hr. All the EIS experiments were performed using Auto FRA, Modular in the frequency range 0.1 Hz-10 MHz with constant amplitude of 10 mV.

2.3 Results and Discussion

2.3.1 Morphological characterizations

The morphologies of the prepared samples are observed by Field emission scanning electron microscopy (FESEM) and Transmission Electron Microscopy (TEM). Fig. 2.2a and b reveal particle-like morphology of Co_3O_4. In Ti_3C_2/Co_3O_4, the Co_3O_4 nanoparticles are decorated over the layers of $Ti_3C_2NH_4T_x$ as can be seen from the FESEM images in fig. 2.2c-f. HRTEM images of $Ti_3C_2NH_4T_x$ depicted in fig. 2.3a and b indicate the layered structure of $Ti_3C_2NH_4T_x$ with interplanar spacing of 1.24 nm (fig. 2.3c), equivalent to HF etched Ti_3C_2 intercalated with Na [22]. Few layered $Ti_3C_2NH_4T_x$ is evident from fig. 2.3a. The diffused SAED ring pattern depicted in the inset of fig. 2.3c suggests decrease in crystallinity of MXene after etching. Etching can cause structural defects, adatoms and vacancies which decreases the overall crystalline order in the long range. Intercalation of DMSO may result in localized distortions. Also, delamination of multilayered Ti_3C_2 may cause lattice defects and irregularities as layers get separated. Thus, crystallinity might get compromised because of these processes. From the HRTEM images of Ti_3C_2/Co_3O_4 (shown in fig. 2.3d and e) it can be confirmed that the Co_3O_4 nanoparticles are distributed over the surface of MXene sheets. Different lattice fringes corresponding to (001) plane [23] and (100) plane) [24] of Ti_3C_2 and (111) plane [25] of Co_3O_4 nanoparticles are observed in fig. 2.3d, which confirms the formation of their crystal structure.

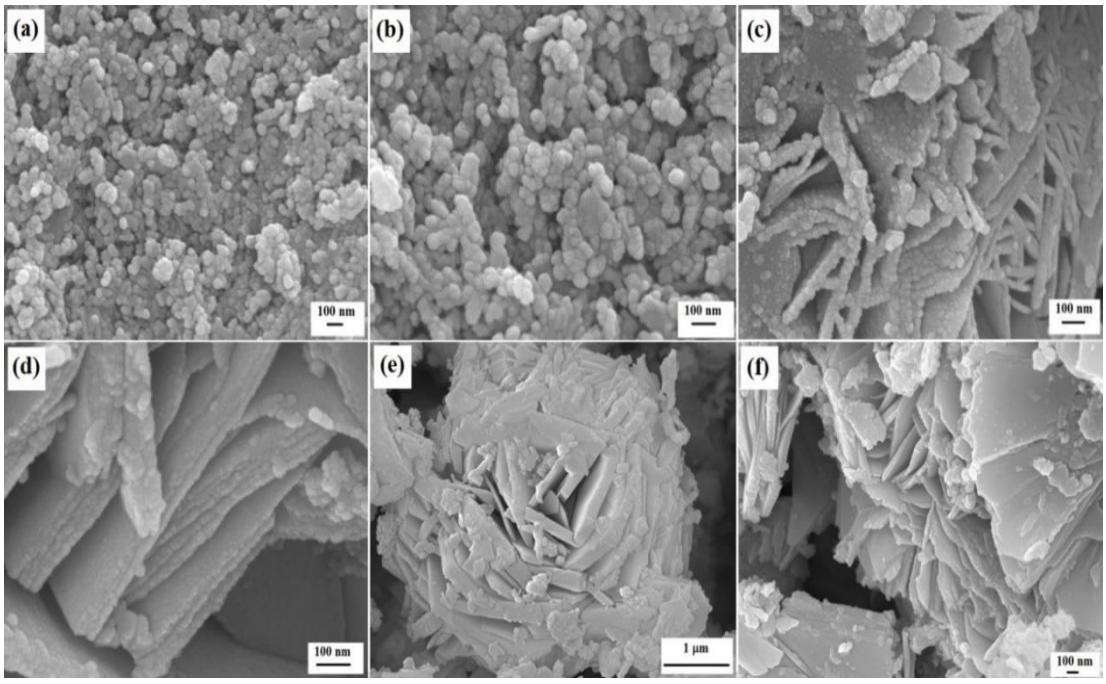

Figure 2.2: FESEM images of (a), (b) Co_3O_4 nanoparticles; (c)-(f) Ti_3C_2/Co_3O_4

From the FESEM images of fig. 2.2c-f, it is observed that the distance between MXene layers increases due to the removal of Al, which is consistent with the minimum Al composition obtained in the EDX spectrum (fig. 2.3f and g).

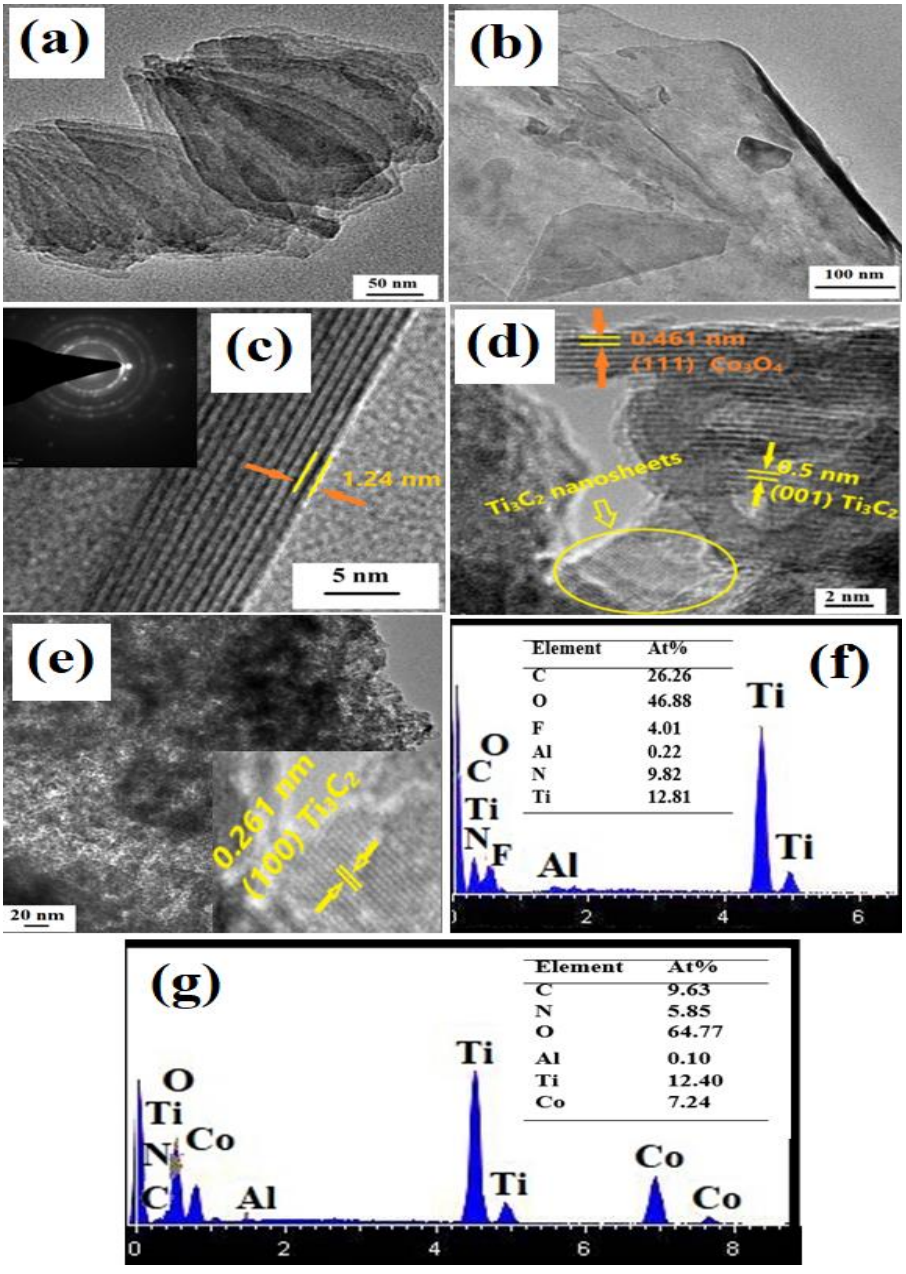

Figure 2.3: (a)-(b) TEM images of $Ti_3C_2NH_4T_x$ nanosheets, (c) Lattice fringes (Inset-SAED pattern) of Ti_3C_2 nanosheets, (d)-(e) TEM images of Ti_3C_2/Co_3O_4. (Inset in fig. 2.3e is the lattice fringes of Ti_3C_2 nanosheets shown inside circle in fig. 2.3d), EDX spectra of (f) Ti_3C_2, and (g) Ti_3C_2/Co_3O_4

A slight amount of Al is present in $Ti_3C_2NH_4T_x$ which is mainly due to the formation of co-products. In $Ti_3C_2NH_4T_x$, besides the presence of Ti, Al, and C; F and N are also present in the form of co-products (explained in eqn. 2.1-2.3). Moreover, presence of O in MXene nanosheets is observed which is due to the presence of -OH groups on the MXene surface. The EDX spectrum of Ti_3C_2/Co_3O_4 in fig. 2.3g confirms the presence of Ti, C, O, Co, Al, N in the nanocomposite. The amount of O increases in Ti_3C_2/Co_3O_4 in comparison to MXene because of the adhesion of Co_3O_4 nanoparticles in addition to the presence of -OH groups on the surface of Ti_3C_2.

2.3.2 Physical characterizations

2.3.2.1 X-ray Diffraction (XRD)

The crystalline structures are studied by X-ray diffraction. In fig. 2.4(i) crystalline peaks can be observed at 9.53°, 19.13°, 33.95°, 35.9°, 39°, 41.75°, 48.37°, 52.39°, 56.41°, and 60.3° which correspond to the (002), (004), (101), (103), (104), (105), (107), (108), (109), and (110) planes, respectively of the MAX Ti_3AlC_2 (JCPDS Card no: 01-074-8806) [26]. After etching Ti_3AlC_2 by NH_4HF_2 (fig. 2.4 (ii)), the Al layers get removed selectively, as a result of which the peak at 39° corresponding to (104) plane disappears.

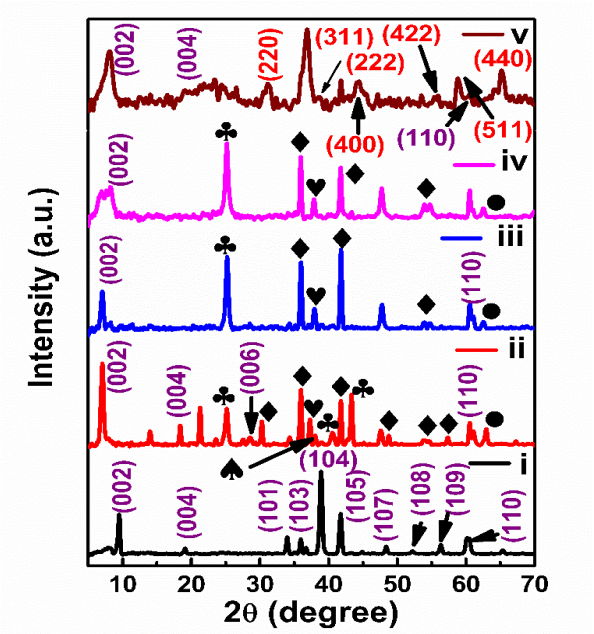

Figure 2.4: XRD patterns of (i) Ti_3AlC_2, (ii) $Ti_3C_2NH_4T_x$, (iii) DMSO intercalated $Ti_3C_2NH_4T_x$, (iv) delaminated $Ti_3C_2NH_4T_x$, and (v) Ti_3C_2/Co_3O_4. (Symbols signifying: ♣ AlF_3, ♦ $(NH_4)_3AlF_6$, ♥ $AlF_3.3H_2O$, ♠ $(NH_4)AlF_4$ and ● TiO_2)

This disappearance of (104) plane suggests the vanishing of MAX Ti_3AlC_2 phase and development of MXene Ti_3C_2 phase [26]. The shift of the peak corresponding to the (002) plane from 9.53° to 7.1° [27] provides further indication of the formation of the MXene phase. This shift to lower 2θ value is because of the increase in interplanar spacing from 9.27 Å to 12.44 Å (which is also evident from the lattice fringes of fig. 2.3c), implying increased c-lattice parameter of Ti_3C_2 to 24.88 Å from 18.54 Å. From the increase in c-lattice parameter, the removal of Al layer and successful formation of MXene phase can be inferred. The interplanar distance increases when the cation of etchant ammonium bifluoride, NH_4^+, intercalates into the layers of Ti_3C_2. The enlarged c-lattice parameter obtained in this work due to NH_4^+ intercalation is comparable to or even larger than that reported in literature using HF etchant followed by different intercalants [28]. Moreover, the peak corresponding to (004) plane gets shifted from 19.1° to 18.4° in MXene, further confirming the formation of Ti_3C_2. Additionally, diffraction peaks corresponding to Ti_3C_2 are observed at 14°, 21.2°, 28.6°, 47.5° and 60.5° [29, 30]. The peaks at 28.6° and 60.5° correspond to (006) and (110) planes of Ti_3C_2, respectively; whereas, the planes of Ti_3C_2 corresponding to peaks at 14°, 21.2° and 47.5° are not known so far in literature [29, 30]. Some additional peaks are observed in $Ti_3C_2NH_4T_x$ (fig. 2.4 (ii)) which arises because of the presence of co-products formed during etching process. They are: 25.4°, 40.4° and 43.3° arising due to AlF_3; 30°, 36°, 41.9°, 49°, 54.4° and 57.3° suggesting the product $(NH_4)_3AlF_6$; 37.4° because of $AlF_3.3H_2O$, and 38° corresponding to $(NH_4)AlF_4$ [31]. The formation of these co-products is explained in equations 2.1-2.3. During the etching process, partial oxidation of Ti_3C_2 takes place and anatase TiO_2 is formed, which is confirmed by the XRD peaks at 38° and 63° [32]. However, this oxidation is very weak which is in consistency with FTIR results. DMSO was intercalated to observe any increase in d-value of $Ti_3C_2NH_4T_x$. However, the d-value cannot be increased further after intercalating and delaminating NH_4HF_2 etched MXene as can be seen in fig. 2.4(iii) and 2.4 (iv). Thus, NH_4HF_2 etchant is safer and allows one to obtain larger d value in one go without using further intercalants. Fig. 2.4 (v) depicts the diffraction peaks of the nanocomposite Ti_3C_2/Co_3O_4. All the diffraction peaks of Co_3O_4 are observed at 2θ value of 31°, 37°, 38.7°, 44.3°, 55.7°, 59°, and 65.2° suggesting the formation of planes (220), (311), (222), (400), (422), (511), (440), respectively [33]. The XRD peak of Co_3O_4 at 19.13°, which corresponds to the (111) plane, broadens and becomes visible as a hump rather than a sharp peak when it merges with the diffraction peak of the (004) plane of

$Ti_3C_2NH_4T_x$. The (002) plane of Ti_3C_2 shifts to a higher value (8°) following the in-situ production of Co_3O_4 in the presence of $Ti_3C_2NH_4T_x$. This is mostly because of the removal of the intercalating ions NH_4^+ present inside the layers of Ti_3C_2. 25 M NaOH used in the synthesis method prevents the oxidation of Ti_3C_2 to anatase TiO_2.

$$Ti_3AlC_2 + NH_4HF_2 \rightarrow (NH_4)_3AlF_6 + AlF_3 + H_2 + Ti_3C_2 \quad (2.1)$$

$$AlF_3 + 3H_2O \rightarrow AlF_3.3H_2O \quad (2.2)$$

$$Ti_3C_2 + NH_4HF_2 + H_2O \rightarrow Ti_3C_2NH_4T_x \quad (2.3)$$

Here T represents the terminals -F and -OH groups.

2.3.2.2 Fourier transform infrared spectroscopy (FTIR)

The chemical compositions of the samples are further established by FTIR spectra depicted in fig. 2.5. The FTIR spectra of MAX phase (Ti_3AlC_2) and MXene are presented in fig 2.5a. The FTIR spectrum of Ti_3AlC_2 is shown separately at lower and higher wavenumber region in fig. 2.5b and 2.5c, respectively. The absorption bands lying between 400-600 cm^{-1} (in fig. 2.5b) are characteristics of Al-O, Ti-O and Ti-C vibrational bonds present in Ti_3AlC_2 [26, 34]. The absorption peaks at 1627 and 3404 cm^{-1} in fig. 2.5c appear due to the presence of –OH vibrational bond. Peaks at 2104, 2345 cm^{-1} are ascribed to Al-OH stretching vibration. Moreover, the C-C and C-O vibrations are responsible for absorption bands that show up in the 1200-1500 cm^{-1} region. After etching, the disappearance of Al-OH stretching vibration in the FTIR spectrum of $Ti_3C_2NH_4T_x$ (shown in fig. 2.5a) confirms the successful removal of Al layer from Ti_3AlC_2. During the etching process, -OH groups get attached to the surface of Ti_3C_2 which can be inferred from the absorption peak of $Ti_3C_2NH_4T_x$ at 562 cm^{-1} (shown in fig. 2.5a), which results from the deformation vibration of Ti-O [35]. Presence of -O terminals on the Ti_3C_2 surface can be confirmed from the absorption peak arising at 1056 cm^{-1} due to the C-O stretching vibration [36]. Additional peaks at 1632, 3069, 3286 cm^{-1} arises due to -OH groups terminated on Ti_3C_2 surface [35]. The oxidation of Ti_3C_2 into anatase TiO_2 is very limited as no prominent absorption peak of anatase TiO_2 phase can be observed. From the FTIR spectrum of Co_3O_4 nanoparticles in fig. 2.5d, the spinel structure can be confirmed by the absorption peaks at 563 and 661 cm^{-1} attributed to OB_3 and ABO vibrations, respectively (with B representing Co^{3+} in octahedral site and A representing Co^{2+} occupying tetrahedral site) [37]. The peak at 1383 cm^{-1} arises due to the stretching vibration of NO_3^- ion [37] and the absorption at 1642 and 3465 cm^{-1}

corresponds to the bending and stretching of H_2O molecules adsorbed on the surface. In the FTIR spectrum of nanocomposite Ti_3C_2/Co_3O_4 shown in fig. 2.5d, the peak at 562 cm^{-1} of Ti_3C_2 merges with the absorption band of Co_3O_4 at 563 cm^{-1}. The observation of all other absorption peaks of Ti_3C_2 in the nanohybrid indicates that its chemical structure remains unaltered during in-situ synthesis of Co_3O_4, hence preventing the oxidation of Ti_3C_2 into TiO_2. The absorption bands of Ti_3C_2 at 1632 and 3286 cm^{-1} merge with the absorption bands of Co_3O_4 at 1642 and 3465 cm^{-1}, respectively and hence broad peaks are observed in the spectra of Ti_3C_2/Co_3O_4.

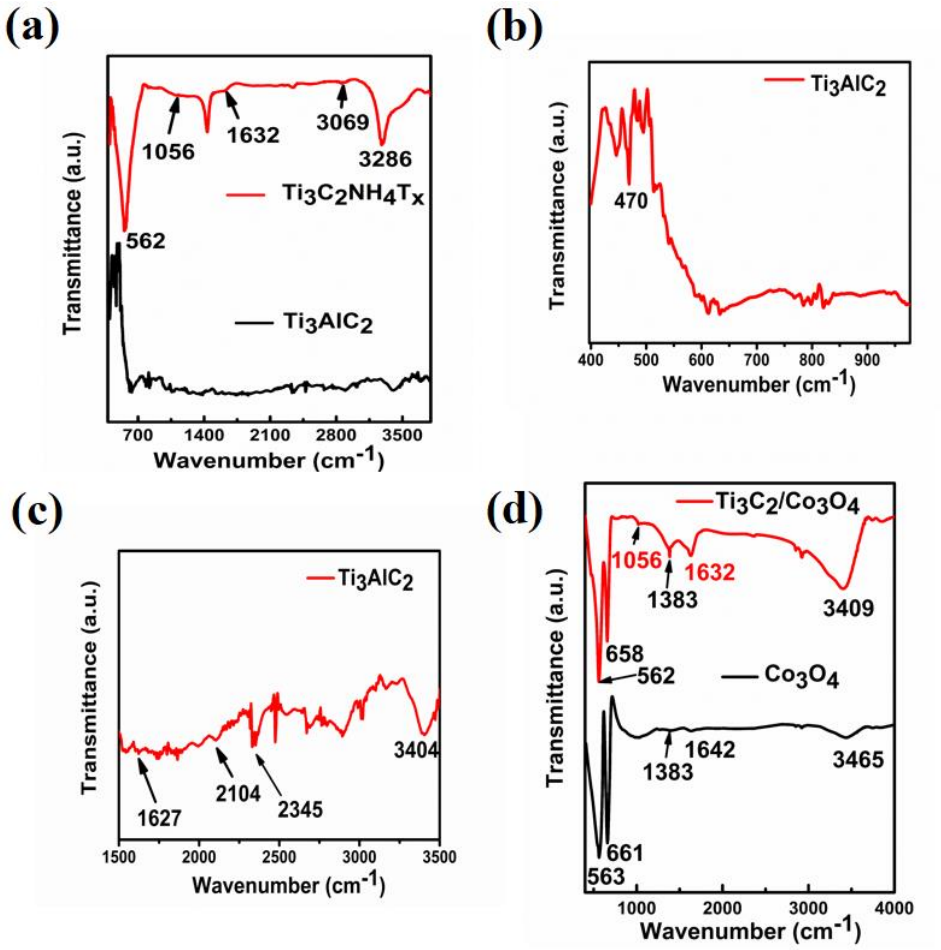

Figure 2.5: FTIR of (a) Ti_3AlC_2 and $Ti_3C_2NH_4T_x$, (b)-(c) Ti_3AlC_2, (d) Co_3O_4 nanoparticles and nanocomposite Ti_3C_2/Co_3O_4

2.3.2.3 X-ray photoelectron spectroscopy (XPS)

To verify the elemental composition and oxidation states in pristine Co_3O_4 and nanocomposite Ti_3C_2/Co_3O_4, XPS was performed. The survey spectrum of Ti_3C_2/Co_3O_4 in fig. 2.6a confirms the presence of Ti, C, Co, O as the main constituting elements along

with N in low concentration. In the high-resolution Co 2p spectrum of Co_3O_4 shown in fig. 2.6b, two large peaks can be seen at around 780 eV and 795 eV. These peaks are caused by the spin-orbit splitting of the 2p orbital into $2p_{3/2}$ and $2p_{1/2}$, respectively. On deconvolution, each such peak comprises of two peaks, yielding four peaks at 779.89, 781.1, 794.9, and 796.4 eV which correspond to Co^{3+} $2p_{3/2}$, Co^{2+} $2p_{3/2}$, Co^{3+} $2p_{1/2}$, and Co^{2+} $2p_{1/2}$, respectively [38]. Whereas, in the nanocomposite Ti_3C_2/Co_3O_4 (fig. 2.6c), the charge transfer from Co_3O_4 nanoparticles to MXene nanosheets causes shift in the peak to higher values i.e. 780.1, 781.6, 795.2, and 796.7 eV. Furthermore, in the survey spectrum, the peak intensity of O 1s in Ti_3C_2/Co_3O_4 is higher than that of Co_3O_4, which is mainly due to the presence of more oxygen-containing species in the nanocomposite as compared to pristine Co_3O_4.

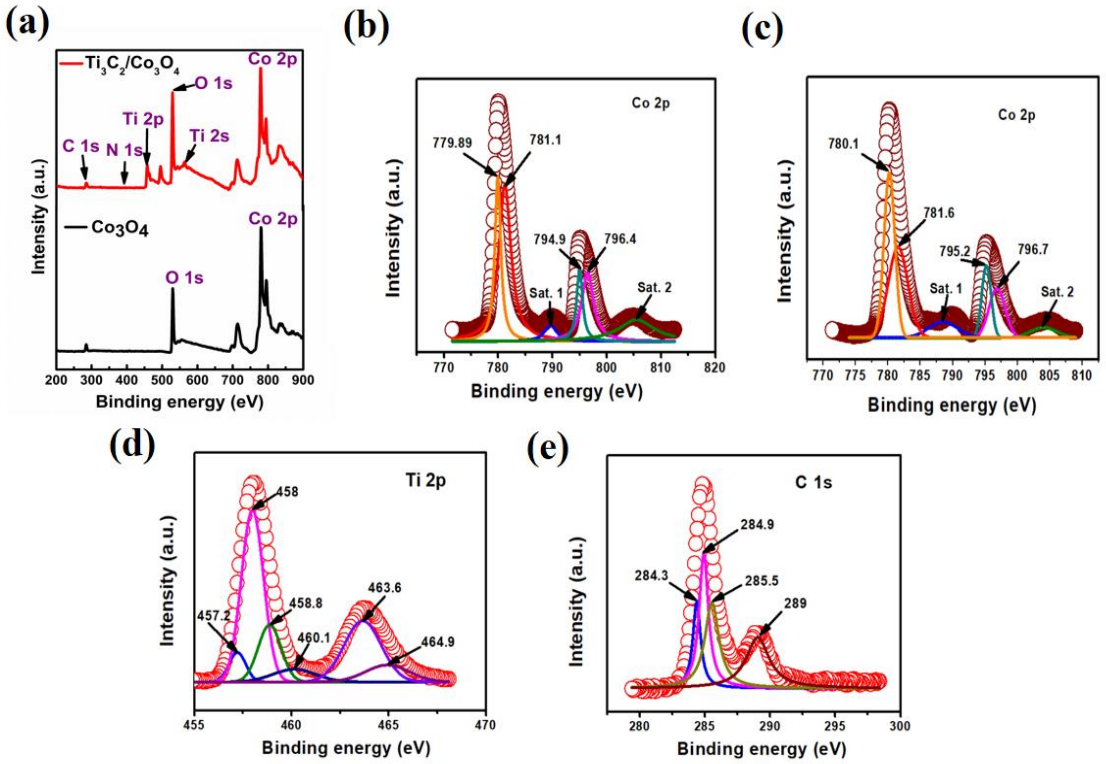

Figure 2.6: (a) XPS survey spectra of Co_3O_4 and nanocomposite Ti_3C_2/Co_3O_4; High resolution XPS spectra of Co 2p in (b) Co_3O_4, and (c) Ti_3C_2/Co_3O_4; High resolution spectra of (d) Ti 2p, and (e) C 1s of nanocomposite Ti_3C_2/Co_3O_4

The high-resolution spectrum of Ti 2p in the nanocomposite (fig. 2.6d) demonstrates Ti $2p_{3/2}$ at around 458 eV and Ti $2p_{1/2}$ around 463 eV. These peaks when deconvoluted reveal 6 peaks (fig. 2.6d) which correspond to different interactions namely, Ti ($2p_{3/2}$) -C (457.2

eV), Ti ($2p_{3/2}$)-Ti ($2p_{3/2}$) (458 eV), Ti ($2p_{3/2}$)-O (458.8 eV), Ti ($2p_{1/2}$)-Ti ($2p_{1/2}$) (460.1 eV), C-Ti ($2p_{1/2}$) -T_x (463.6 eV), and Ti ($2p_{1/2}$)-O (464.9 eV) [39, 40], with T_x being the hydrophilic terminations. The C 1s spectrum (fig. 2.6e) of Ti_3C_2/Co_3O_4 is resolved into four peaks at 284.3, 284.9, 285.5, and 289 eV reflecting the C-C, C-N, CH_x/C-O, and C=O interactions, respectively [40]. From the C-N interaction, the presence of N containing co-products of Ti_3C_2 etching can be established.

2.3.2.4 Nitrogen (N_2) adsorption-desorption analysis

The surface area and porosity are studied by Brunauer–Emmett–Teller (BET). Figure 2.7 shows the N_2 adsorption-desorption isotherms derived from BET as well as the inset of the Barrett-Joyner-Halenda (BJH) pore size distribution. All of them i.e., Ti_3C_2, Co_3O_4 and Ti_3C_2/Co_3O_4 exhibit type IV isotherm and H3 hysteresis loop, suggesting the presence of mesopores in all the samples. Ti_3C_2 nanosheets have an average mesopore size of 3.6 nm and a specific surface area of 23.2 m^2/g.

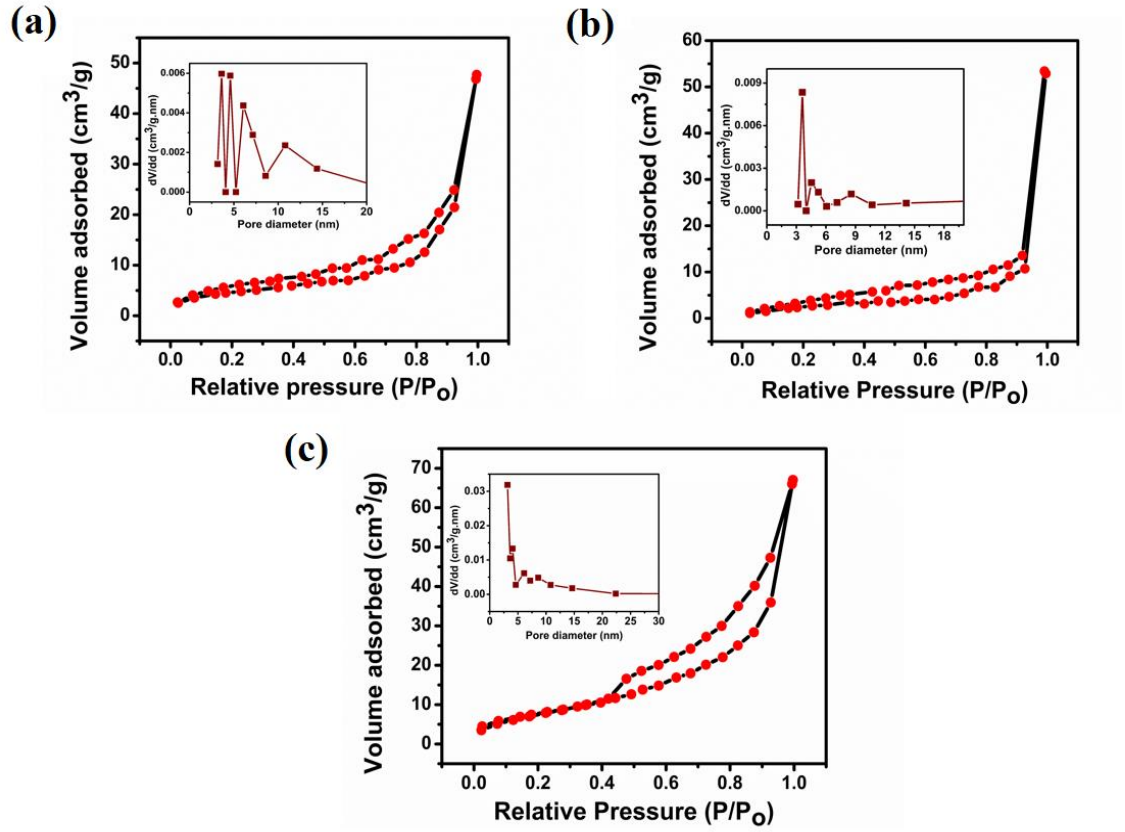

Figure 2.7: N_2 adsorption-desorption isotherms of (a) Ti_3C_2, (b) Co_3O_4 and (c) Ti_3C_2/Co_3O_4. Inset-Pore size distribution curves of the corresponding samples

Co_3O_4 nanoparticles with pore size of 3.5 nm has lesser surface area (17.906 m^2/g) than Ti_3C_2; whereas the surface area of nanocomposite Ti_3C_2/Co_3O_4 increases to 47.583 m^2/g after incorporating Co_3O_4 to MXene nanosheets. Additionally, the nanocomposite has mesopores with an average size of around 3.14 nm. The development of the nanocomposite Ti_3C_2/Co_3O_4 reduces the agglomeration of Co_3O_4 nanoparticles and also minimizes the restacking of Ti_3C_2 nanosheets, leading to enhanced electrocatalytic activity of the nanocomposite due to the synergistic effect of the individual components.

2.3.3 Electrochemical characterizations

2.3.3.1 Electrochemical activity of the electrodes in absence of methanol

The electrochemical activities of the electrodes are studied in alkaline electrolyte 0.5 M NaOH solution and presented in fig. 2.8. The cyclic voltammetry of Co_3O_4/GC at scan rate of 20 mV/s is depicted in Fig. 2.8a.

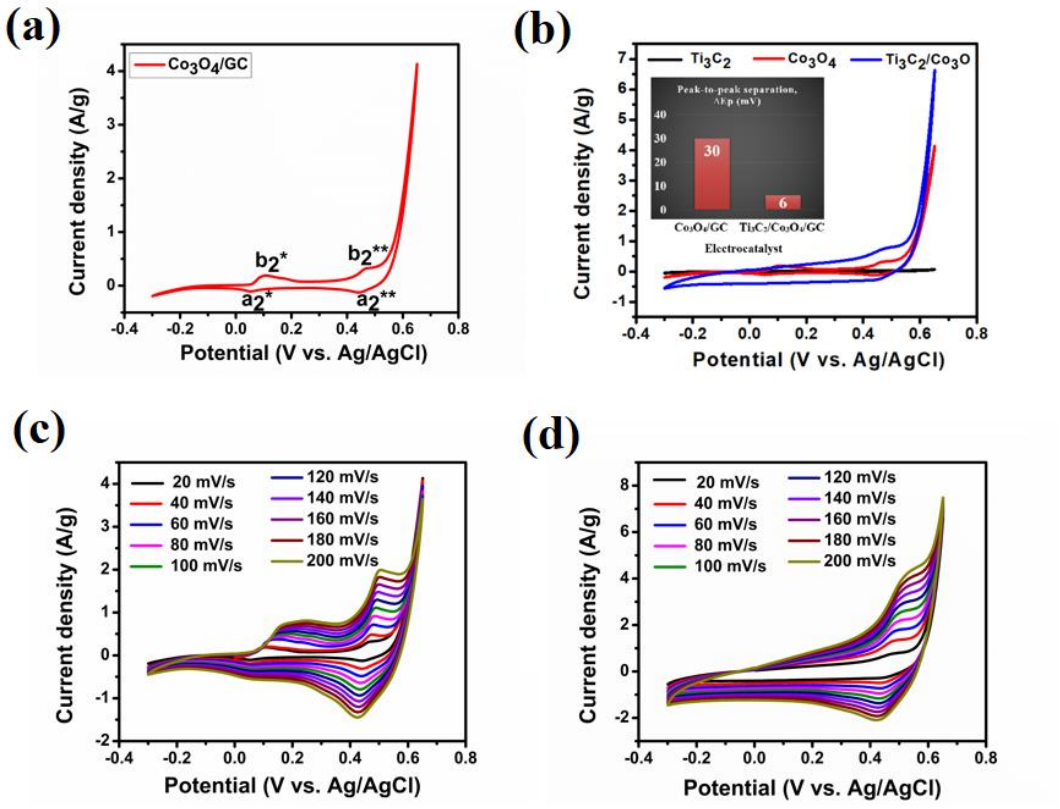

Figure 2.8: Electrochemical behaviour of the electrodes in 0.5 M NaOH solution (absence of methanol)-Cyclic voltammetry of (a) Co_3O_4/GC at 20 mV/s scan rate, (b) Ti_3C_2/GC, Co_3O_4/GC and Ti_3C_2/Co_3O_4/GC at 20 mV/s scan rate (Inset: Peak-to-peak separation graph at 20 mV/s scan rate), (c) Co_3O_4/GC at (20-200) mV/s scan rate, (d) Ti_3C_2/Co_3O_4/GC at (20-200) mV/s scan rate

Two redox couples (b_2^*/a_2^*) and (b_2^{**}/a_2^{**}) are observed which correspond to the oxidation and reduction of Co_3O_4 in presence of OH^- ions of NaOH solution [41]. The redox reactions corresponding to these peaks are explained in equations 2.4-2.7.

$$b_2^* \qquad Co_3O_4 + OH^- + H_2O \rightarrow 3CoOOH + e^- \tag{2.4}$$

$$b_2^{**} \qquad CoOOH + OH^- \rightarrow CoO_2 + H_2O + e^- \tag{2.5}$$

$$a_2^{**} \qquad CoO_2 + H_2O \rightarrow CoOOH + OH^- \tag{2.6}$$

$$a_2^* \qquad 3CoOOH + e^- \rightarrow Co_3O_4 + OH^- + H_2O \tag{2.7}$$

Figure 2.8b shows the CVs of the electrodes Ti_3C_2/GC, Co_3O_4/GC, and Ti_3C_2/Co_3O_4/GC in 0.5 M NaOH solution at 20 mV/s scan rate. MXene Ti_3C_2 does not show any redox peaks due to the absence of electroactive sites in it. Nonetheless, various redox peaks are seen in Co_3O_4/GC and Ti_3C_2/Co_3O_4/GC, which correspond to distinct oxidation states of Co. In pristine Co_3O_4 two redox couples (b_2^*/a_2^*) and (b_2^{**}/a_2^{**}) are detected as shown in fig. 2.8a and explained by eqns. 2.4-2.7), whereas in Ti_3C_2/Co_3O_4, only one redox pair (b_2^{**}/a_2^{**}) corresponding to +3/+4 is prominent. This suggests that the majority of the Co in the nanocomposite is present in the +3 state. Tabel 2.1 lists the anodic peak potential (E_p), current density (I_p) and peak-to-peak separation (ΔE_p) of the electrodes at 20 mV/s. Figure 2.8b displays the ΔE_p value as an inset. Figures 2.8c and 2.8d show that Ti_3C_2/Co_3O_4/GC has larger anodic current densities than Co_3O_4/GC. Enlarged CV area and higher anodic peak current density of Ti_3C_2/Co_3O_4/GC than Co_3O_4/GC signify better electrochemical ability of the nanocomposite, which originates from the synergistic effect of the individual components. High surface area of MXene enables more Co_3O_4 nanoparticles to disperse on a largely exposed surface leading to the exposure of more active sites. Moreover, the conductivity of MXene fastens the charge transfer process resulting in higher current density. Thus, reason behind superior electrochemical performance of the 2D hybrid nanosystem Ti_3C_2/Co_3O_4 can be attributed to its capacity to provide more active sites owing to its 2D structure and additional sites due to the interface between 2D and 0D nanostructures. The CVs of the electrodes in 0.5 M NaOH with scan rate ranging between 20-200 mV/s are displayed in fig. 2.8c and 2.8d. It can be observed that the anodic (I_{pa}) and cathodic (I_{pc}) peak current density increases with increase in scan rate (ν), and the anodic peaks shift towards more positive value, whereas, the cathodic peaks shift towards negative potential. This shift occurs because of quasi-reversibility of the redox reactions indicating the hindrance in charge transfer arising due

to the chemical reactions taking place between the electrolyte ions and the electrodes. It raises the internal resistance of the electrodes.

Table 2.1: Anodic peak potential, peak current density and peak-to-peak separation of the electrodes at 20 mV/s scan rate

Electrocatalyst	Anodic peak potential, E_{pa} (V)	Anodic peak current density, I_{pa} (A/g)	Peak-to-peak separation, ΔE_p (mV)
Co_3O_4/GC	0.470	0.33	30
Ti_3C_2/Co_3O_4/GC	0.479	0.78	6

The variation of peak-to-peak separation, ΔE_p with scan rate signifies the type of electrochemical reaction taking place on the electrode surface [42]. For Co_3O_4/GC, ΔE_p is less than 59 mV within scan rate 20-100 mV/s and the ratio I_{pa}/I_{pc} approaches unity, which reveals reversibility of the chemical reactions [43]. Conversely, as ν rises beyond 100 mV/s, the electron transfer kinetics slows down due to the faster rate of change of potential, leading to an increase in the ΔE_p value in the range (120-200) mV/s. It implies quasi-reversibility of the electron transfer process taking place on Co_3O_4/GC [42, 43]. The nanocomposite Ti_3C_2/Co_3O_4 maintains this reversibility for lower scan rate (20-80) mV/s, beyond which the reactions become quasi-reversible. At 20 mV/s scan rate, Ti_3C_2/Co_3O_4/GC offers smaller peak-to-peak separation of 6 mV as compared to Co_3O_4/GC offering 30 mV. It is mainly due to the conductive network created by Ti_3C_2 for the Co_3O_4 nanoparticles, thus suggesting improved reversibility of electrode Ti_3C_2/Co_3O_4/GC. The linear dependence of the peak current density on the scan rate (ν) (fig. 2.9a, b) suggests the electrochemical behaviour of the surface adsorbed redox couple Co^{+3}/Co^{+4} in both Co_3O_4 and Ti_3C_2/Co_3O_4 [44]. The peak current densities of Co_3O_4/GC and Ti_3C_2/Co_3O_4/GC show a linear dependence on the square root of ν at higher scan rates (as shown in fig. 2.9c, d) indicating the free diffusion of electroactive molecules towards the electrodes [45].

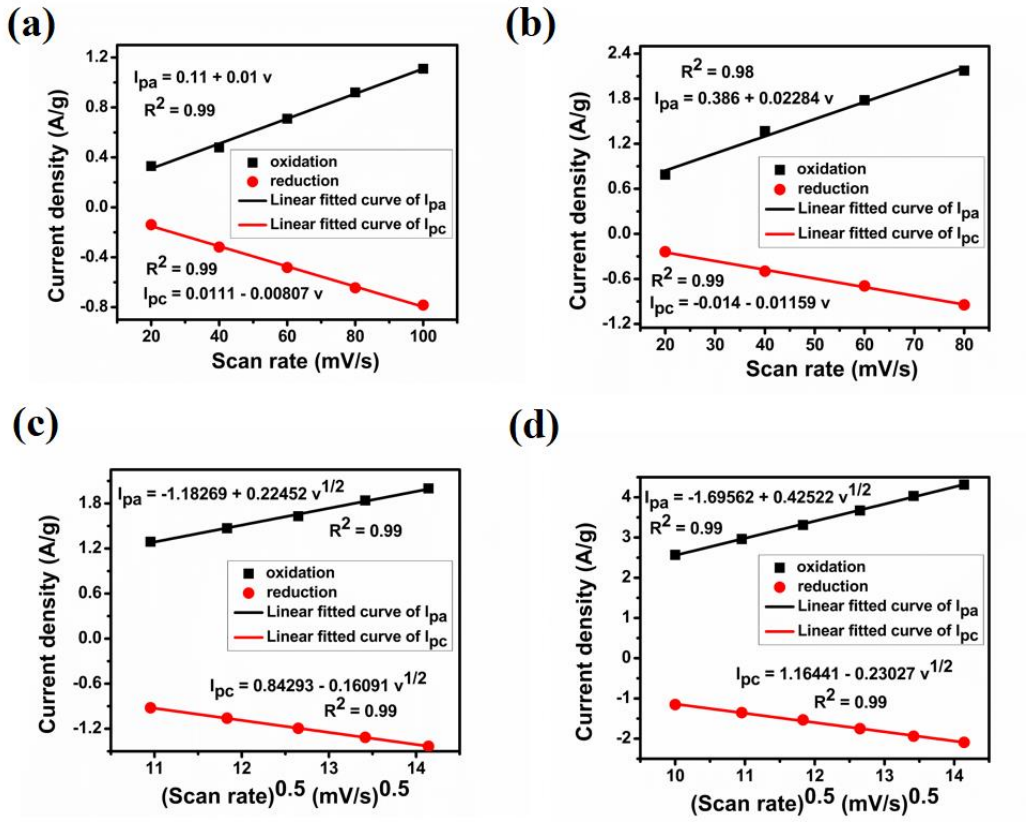

Figure 2.9: (a), (b): I_p vs. ν plot of Co_3O_4/GC and Ti_3C_2/Co_3O_4/GC respectively. (c), (d): I_p vs. $v^{1/2}$ plot of Co_3O_4/GC and Ti_3C_2/Co_3O_4/GC respectively

Thus, both the diffusion and surface confined processes are taking place, which lead to improved electrochemical property of the electrodes. As depicted in fig. 2.10a, the slope of the straight line in log I_p vs. log v plot for both the electrodes lies between 0.5 and 1, which further confirms the presence of both processes in the undergoing electrochemical reactions. The surface coverage (Γ^*) of the redox species can be calculated from the slope of these straight lines (linear fitted I_p vs. ν plot) and using the Brown-Anson model [46], which gives the relation between peak current density with sweep rate, ν as $I_p = \frac{n^2F^2\Gamma^*Av}{4RT}$ where, n represents the number of electrons involved in the process, F is the Faraday constant, A being the geometric surface area of the electrode, R is gas constant and T is the absolute temperature. Taking average of both anodic and cathodic results, the surface coverage of Co_3O_4/GC and TC/GC are calculated to be 4.90×10^{-8} and 9.35×10^{-8} mol/gcm^2. Ti_3C_2 nanosheets provide a larger surface area to the nanocomposite

Ti_3C_2/Co_3O_4, leading to higher Γ* value which is 1.9 times greater than that of Co_3O_4/GC.

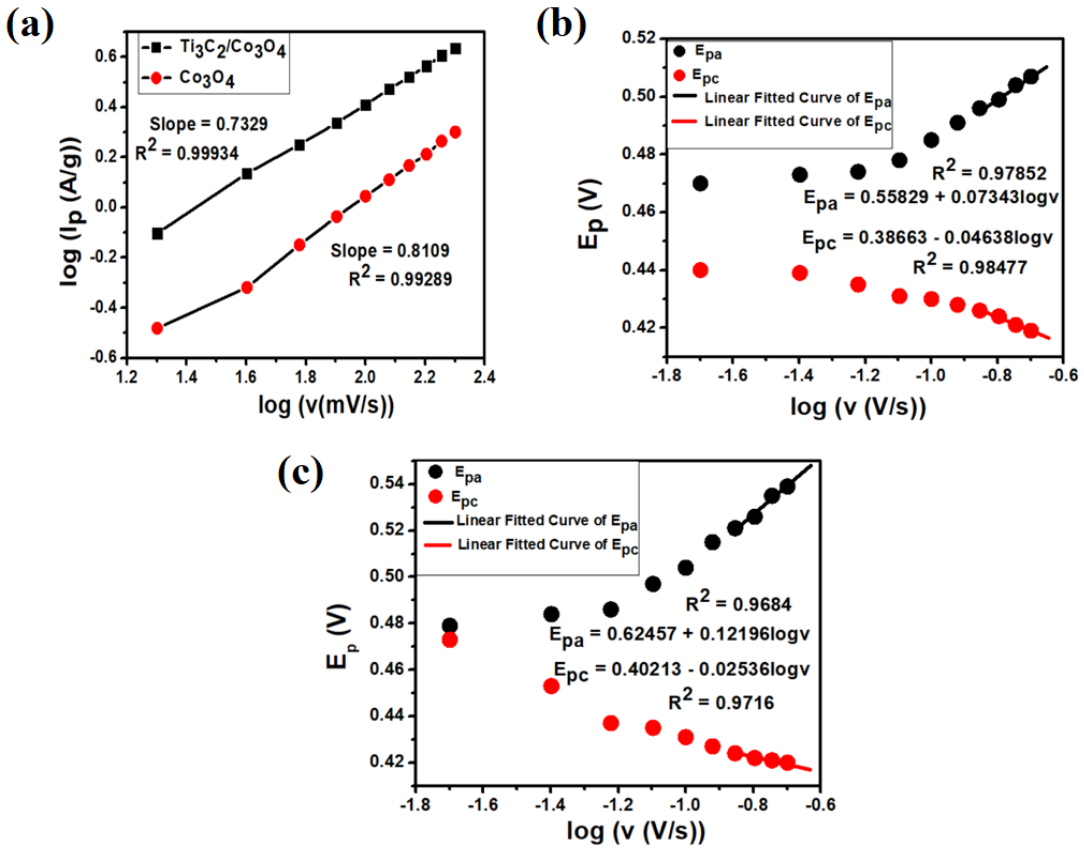

Figure 2.10: (a) Plot of logarithm of peak anode current density vs. logarithm of scan rate, Laviron's plot: Anodic and cathodic peak potential (v) vs logarithm of scan rate (b) Co_3O_4/GC, (c) Ti_3C_2/Co_3O_4/GC

By calculating the electron transfer coefficient (α) and apparent charge transfer rate constant (k_s) using Laviron's method, the kinetics of the processes between the electrode surface and the electrolyte ions may be comprehended [47]. The following equations 2.8-2.10 illustrate the relationship between peak potential (E_p) and the logarithm of scan rate (ν) given by Laviron's method.

$$E_{pa} = E_o + 2.3RT\frac{log\,\nu}{(1-\alpha)nF} \tag{2.8}$$

$$E_{pc} = E_o - 2.3RT\frac{\log\nu}{\alpha nF} \tag{2.9}$$

$$logk_s = \alpha\log(1-\alpha) + (1-\alpha)log\alpha - log\frac{RT}{nF\nu} - \alpha(1-\alpha)\frac{nF\Delta E_p}{2.3RT} \tag{2.10}$$

where E_{pa} and E_{ca} are anodic and cathodic peak potentials respectively, n is the number of electrons transferred and other terms have their usual meanings. The plots of E_p vs. log ν are displayed in fig. 2.10b and c. The anodic charge transfer coefficient (α) was calculated from the slope of E_{pa} [48] and found to be 0.2 and 0.5 for Co_3O_4/GC and Ti_3C_2/Co_3O_4/GC, respectively. The calculated k_s values for Co_3O_4/GC and Ti_3C_2/Co_3O_4/GC are 1.0608 s^{-1} and 1.1403 s^{-1}, respectively. The higher α and k_s value of Ti_3C_2/Co_3O_4/GC than Co_3O_4/GC implies faster reaction kinetics of the nanocomposite because of the conductive network created by MXene nanosheets for the Co_3O_4 nanoparticles. Additionally, it reduces the aggregation of Co_3O_4 nanoparticles and increases the rate of charge transfer from Co_3O_4 to MXene nanosheets. The obtained k_s values are higher than reported works [49, 50], which makes the developed electrodes a potential candidate for electrocatalysis.

2.3.3.2 Electrochemical activity of the electrodes in presence of methanol

Cyclic voltammetry is used to understand the catalytic activity of the prepared electrodes towards oxidation of methanol. Figure 2.11a displays the cyclic voltammograms of each electrode in 1.5 M methanol solution containing 0.5 M NaOH as a supporting electrolyte. It is observed that due to the absence of redox active sites in MXene, it does not contribute to methanol oxidation. A methanol oxidation current density of 13.14 A/g (13.4 mA/cm^2) with an onset potential of 0.34 V vs. Ag/AgCl is achieved using Co_3O_4/GC electrode. With a lower onset potential of 0.32 V at a 20 mV/s scan rate, the nanocomposite Ti_3C_2/Co_3O_4/GC demonstrates the highest methanol oxidation current density of 38.38 A/g (20 mA/cm^2). The obtained methanol oxidation current density is higher than recently reported works [51-59]. A comparison is shown in table 2.2 with previous reports. Strong Lewis acid-base interactions between Ti_3C_2 terminations and Co_3O_4 nanoparticles shorten the charge transfer pathway and increase the surface area available for methanol molecules to be adsorbed and oxidized, which explains why Ti_3C_2/Co_3O_4/GC has a greater current density than Co_3O_4/GC. Moreover, the hydrophilic terminations present on MXene surface act as adsorption sites for methanol molecules, leading to increased MOR. Furthermore, the interfaces between Co_3O_4 nanoparticles and MXene nanosheets provided by this hybrid nano system aid in exposing additional active sites, which promotes higher methanol oxidation.

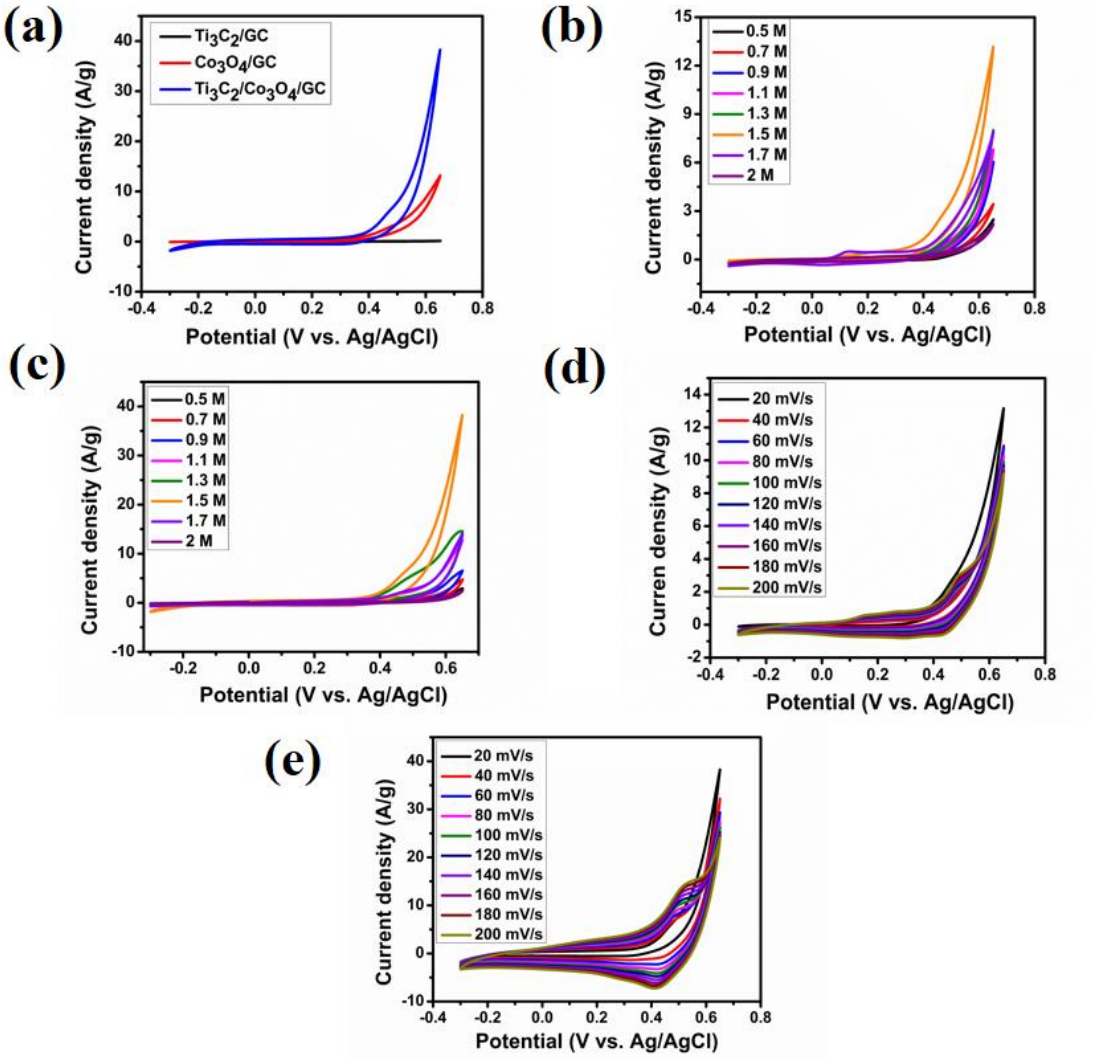

Figure 2.11: Electrochemical behaviour of the electrodes in presence of methanol- Cyclic voltammograms of (a) Ti_3C_2/GC, Co_3O_4/GC, Ti_3C_2/Co_3O_4/GC at 20 mV/s in 0.5 M NaOH solution containing 1.5 M methanol, (b) Co_3O_4/GC, and (c) Ti_3C_2/Co_3O_4/GC in 0.5 M NaOH solution containing varying concentration of methanol at 20 mV/s (d) Co_3O_4/GC in 1.5 M methanol solution with varying scan rate from 20-200 mV/s, (e) Ti_3C_2/Co_3O_4/GC electrode in 1.5 M methanol solution with varying scan rate from 20-200 mV/s

The plausible reaction involved in the oxidation of methanol is explained (in equations 2.11-2.12) below-

$$2CoOOH + 2CH_3OH + 2.5O_2 \rightarrow 2Co(OH)_2 + 2CO_2 + 3H_2O \quad (2.11)$$

$$CoO_2 + CH_3OH \rightarrow CoOOH + product \quad (2.12)$$

The CoOOH (III) obtained from the oxidation of Co_3O_4 (II) (explained in eqn. 2.4) oxidizes methanol to form CO_2 and water. As can be seen in fig. 2.11b and 2.11c, when methanol concentration increases from 0.5 M to 1.5 M, the methanol oxidation current increases, beyond which it decreases. 1.5 M is the critical methanol concentration beyond which the intermediates of methanol oxidation limit the charge occupation of the catalysts. From this, it can be inferred that the methanol oxidation is not a diffusion-controlled process.

Table 2.2: Comparison of the MOR current density of different anode catalysts.

Serial no.	Material (Anode catalyst)	MOR current density	Ref.
1	Ti_3C_2/Co_3O_4	38.38 Ag^{-1} 20 $mAcm^{-2}$	This work
2	$Pd/Ti_3C_2T_x$	12.4 $mAcm^{-2}$	51
3	Pd/MX-rGO	12 $mAcm^{-2}$	52
4	Pt/Ti_3C_2	1.137 $mAcm^{-2}$	53
5	Pt NW/PDDA-$Ti_3C_2T_x$	17.2 $mAcm^{-2}$	40
6	PtRu/MXene	17.2 $mAcm^{-2}$	20
7	Ni/gCN	0.1228 A/g	54
8	Co_3O_4/Ni foam	36.2 A/g	9
9	Pt/G-MoS_2	13.3 $mAcm^{-2}$	55
10	Pt-MoS_2/RGO	7.35 $mAcm^{-2}$	56
11	Pd@C-rGO	3 $mAcm^{-2}$	57
12	Pd-C@MoS_2/RGO	11.2 $mAcm^{-2}$	58
13	PPy-SbW9-TM-SnR/Pt	0.87 $mAcm^{-2}$	59

The effect of scan rate in methanol oxidation reaction is evaluated and illustrated in fig. 2.11d and 2.11e. It has been noted that reduction in methanol oxidation occurs with increasing scan rate. This distinct electrochemical behaviour of the electrodes implies that there occur certain limitations in electrode kinetics at higher scan rate [60]. However, the redox reactions of $Co^{+3} \leftrightarrow Co^{+4}$ do not decelerate with increasing scan rate. The CoOOH oxidation peak current increases and potential shifts towards positive side with

increasing ν. In presence of methanol, the reduction peak of CoO_2 to CoOOH also increases with scan rate. This implies that MOR activity of the electrodes reduces even after the presence of abundant redox sites and the conversion of Co^{+3}/Co^{+4} is favoured more than the methanol oxidation. During higher scan rates the reaction time for methanol oxidation gets reduced, which impedes the transport of electrons from the substrate GCE to the electroactive sites. Further, the reaction intermediates produced during MOR blocks the active sites which further reduces the MOR peak current. In fig. 2.12, the decrease in the reduction peak corresponding to Co^{+4}/Co^{+3} after methanol addition suggests the fact that CoO_2 and CoOOH are consumed more by methanol for oxidation.

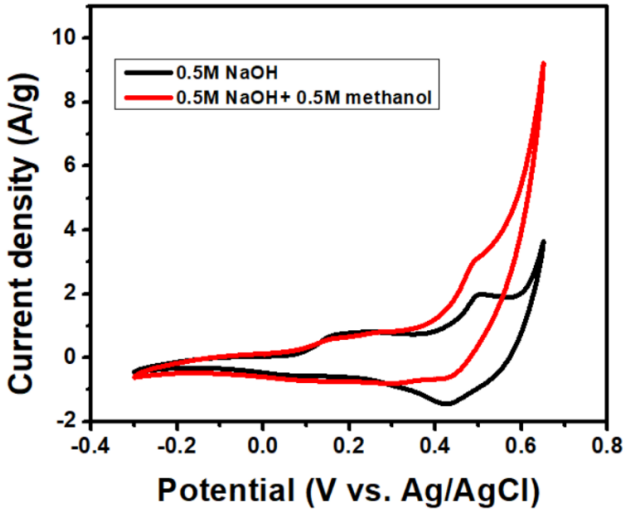

Figure 2.12: Cyclic voltammetry of Co_3O_4/GC in 0.5 M NaOH supporting electrolyte in the presence and absence of 1.5 M methanol at 200 mV/s

The kinetics of the MOR is studied by Tafel plot. The Butler-Volmer equation or the Tafel equation for anodic process is explained as $E_p = \frac{2.303RT}{(1-\alpha)nF}[log\ I_P - log\ I_o]$, where I_p is the MOR current density, I_o is the exchange current density, n denotes the number of electrons involved in the electrode reaction and α is the charge transfer coefficient, E_p is the electrode potential or overpotential [61, 62]. The slope of the plot E_p vs. log I_p is the Tafel slope. A smaller Tafel slope is desirable for a better electrocatalyst and is recommended as the rate-determining step of a multiple-electron reaction [62]. Tafel slope of 241 mV/dec and 192 mV/dec are obtained for Co_3O_4/GC and Ti_3C_2/Co_3O_4/GC, respectively as shown in fig. 2.13a. The lower Tafel slope of Ti_3C_2/Co_3O_4/GC suggests

faster kinetics of methanol oxidation (at 20 mV/s in 1.5 M CH_3OH) than pristine Co_3O_4/GC.

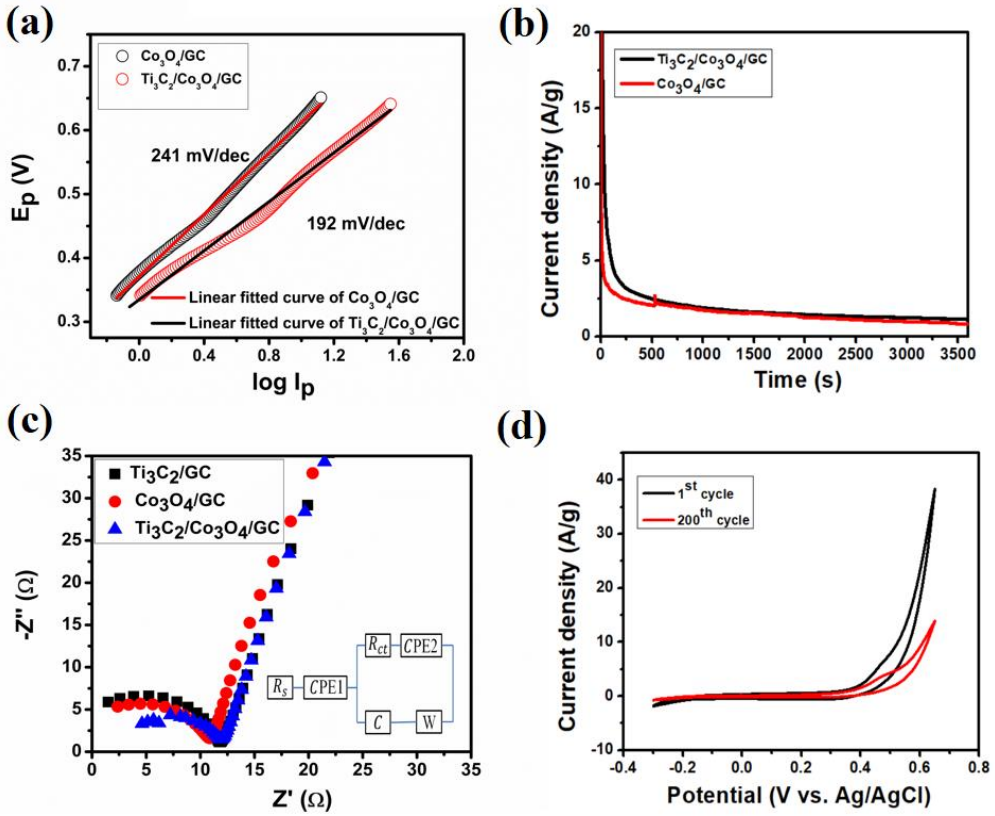

Figure 2.13: (a) Tafel plots of Co_3O_4/GC and Ti_3C_2/Co_3O_4/GC in 1.5 M methanol + 0.5 M NaOH at 20 mV/s, (b) Chronoamperogram of Co_3O_4/GC and Ti_3C_2/Co_3O_4/GC electrodes in 0.5 M NaOH aqueous solution containing 1.5 M methanol at 0.65 V for 3600 s, (c) Nyquist plots of the electrodes, (d) cycling stability of Ti_3C_2/Co_3O_4/GC at 20 mV/s in 1.5 M methanol containing 0.5 M NaOH aqueous solution

To understand the electrochemical stability and activity of the electrodes, the electrodes are assessed using chronoamperometry [63] in 1.5 M methanol solution with 0.5 M NaOH supporting electrolyte for one hour at the peak methanol oxidation potential 0.65V. As displayed in fig. 2.13b, the current drops for the first 250 s for both Ti_3C_2/Co_3O_4/GC and Co_3O_4/GC electrodes and then remain constant at a certain value. The initial decrease is because of the presence of CO intermediates and due to diffusion polarization. Co_3O_4/GC offers deterioration rate of 1.54×10^{-4}, whereas Ti_3C_2/Co_3O_4/GC offers comparatively lesser deterioration rate of 1.50×10^{-4}. Thus, it can be concluded that due to the presence of surface terminations like -O, -F, -OH on MXene surface, good

interfacial contact is built between MXene and Co_3O_4 nanoparticles and prevent the adsorption of CO with the Co_3O_4, which further reduces site-blocking [64]. These -OH ions react with CO intermediates to form CO_2 and help in releasing the active sites from the intermediates, maintaining the durability of the catalysts. Figure 2.13c shows the Nyquist plots used to assess the charge transfer resistances of the electrocatalysts. The Nyquist plots of our catalytic materials are composed of a semicircle at high frequency followed by a straight line with 45° inclination in the lower frequency range. The diameter of this semicircle stands for the charge transfer resistance (R_{ct}), while the straight line suggests the capacitive property of the material. Among the three electrodes, Ti_3C_2/Co_3O_4/GC exhibits the smallest semicircle (R_{ct} =7.45 Ω) which represents rapid electron transfer at the electrode-electrolyte interface resulting from the diffusion-controlled process [65], which is consistent with the CV analysis. The facile penetration of the ions and electrons into the catalysts involved in methanol oxidation results in a lower value of R_{ct}. The R_{ct} values of Ti_3C_2/GC and Co_3O_4/GC are found to be 10.83 Ω and 9.11 Ω, respectively. Higher slope of Ti_3C_2/Co_3O_4/GC Nyquist plot at the lower frequency region suggests capacitive behaviour of the nanocomposite, making it a viable option for use in supercapacitors. The cycling stability of the prepared electrodes is studied by continuous CV cycles as shown in fig. 2.13d. Ti_3C_2/Co_3O_4/GC exhibits stability up to 200 CV cycles conducted in 1.5 M methanol solution at 20 mV/s scan rate with 37% current retention. The decrease in MOR current density is because of the intermediate products of methanol oxidation.

2.3.4 Characterizations of the electrode after cycling stability

The change in morphology and chemical composition of the anode catalyst Ti_3C_2/Co_3O_4 after cycling stability for 200 CV cycles are observed by FESEM and FTIR. As observed in fig. 2.14a-c, the layered structure of $Ti_3C_2NH_4T_x$ becomes restacked and deformed, and the Co_3O_4 nanoparticles get agglomerated after methanol oxidation. The distorted morphology reduces the interfacial contact between Co_3O_4 nanoparticles and MXene nanosheets; as a result of which the redox active sites decrease, leading to reduced methanol oxidation. To observe the structural stability of the catalyst, XRD of Ti_3C_2/Co_3O_4 is done after 200 CV cycles. As displayed in fig. 2.14d, no new phase is found after methanol oxidation. The crystalline peaks of the nanocomposite Ti_3C_2/Co_3O_4 are observed; however, the intensity reduces a bit after continuous cyclic stability.

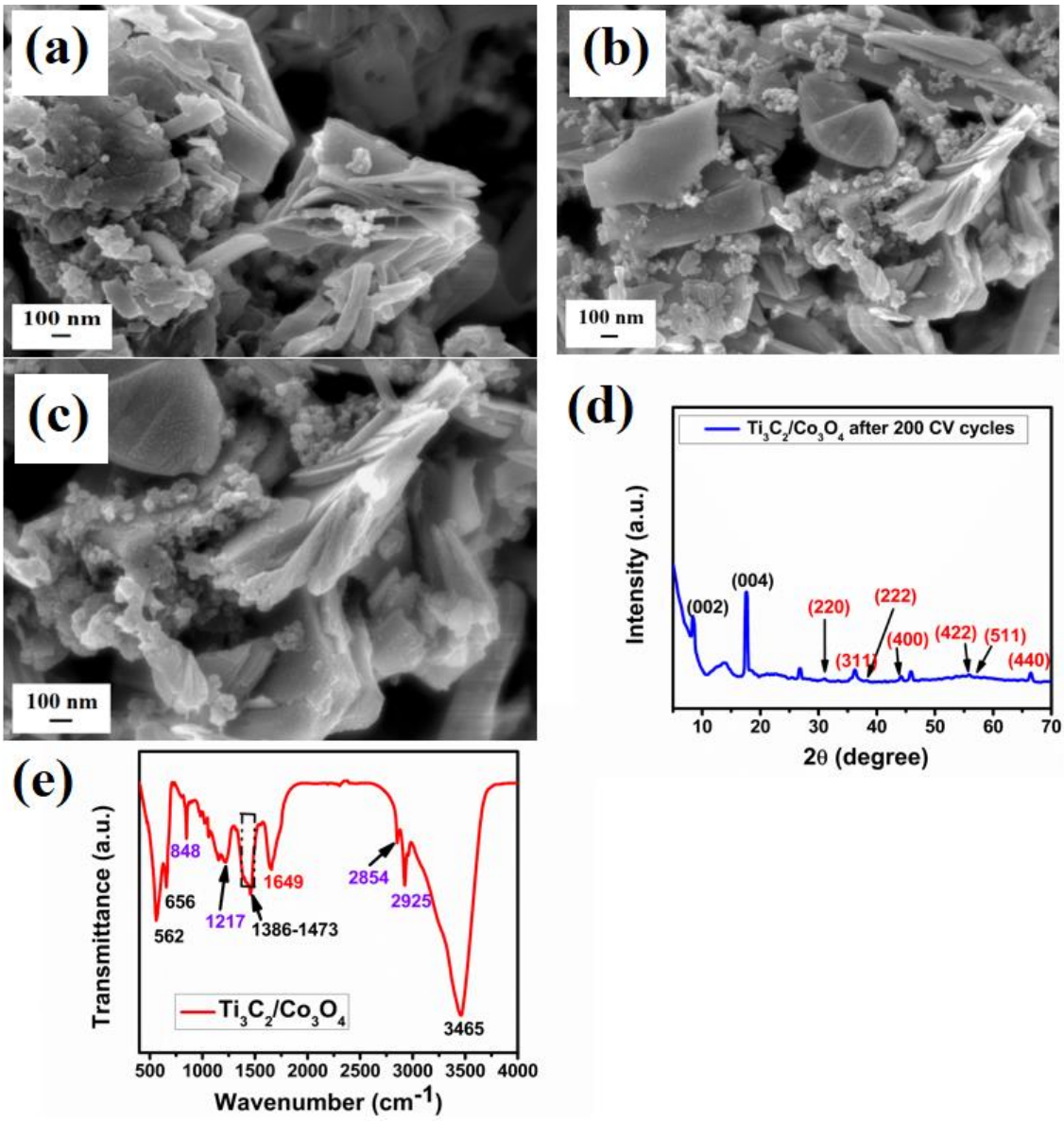

Figure 2.14: (a)-(c) FESEM images, (d) XRD pattern, (e) FTIR spectra of Ti_3C_2/Co_3O_4 after 200 CV cycles in 1.5 M methanol solution containing 0.5 M NaOH aqueous solution

Post methanol oxidation, additional absorption peaks at 848, 1217, 2854, and a strong peak at 2925 cm^{-1} are seen in the FTIR spectrum (shown in fig. 2.14e) of Ti_3C_2/Co_3O_4. The absorption peak at 848 cm^{-1} is associated with the πCO_3 of bidentate carbonate, whereas 1217 cm^{-1} appears due to δOH^{-1} of hydrogen carbonate species formed on the surface of Ti_3C_2/Co_3O_4 [66]. The combination of symmetric CO_2 stretching of adsorbed CO_2 molecules and O-H bending vibrations of surface adsorbed methanol molecules results in a broad absorption band at about 1386-1473 cm^{-1}. The adsorbed methoxy

species give rise to a modest peak at 2854 cm^{-1}, whereas the O-H stretching of the surface adsorbed methanol molecules is responsible for the substantial absorption at 2925 cm^{-1}. Thus, after few cycles of methanol oxidation, the surface of the catalyst is covered with intermediates and the active sites get blocked. This leads to the substantial current drop after 200 CV cycles.

After the stability test, XPS was done to know the changes in chemical states of the catalyst Ti_3C_2/Co_3O_4 after the methanol oxidation process. From fig. 2.15a it can be seen that the intensity of Co and Ti 2p orbitals decreases after methanol oxidation, suggesting the degradation of the catalyst over time.

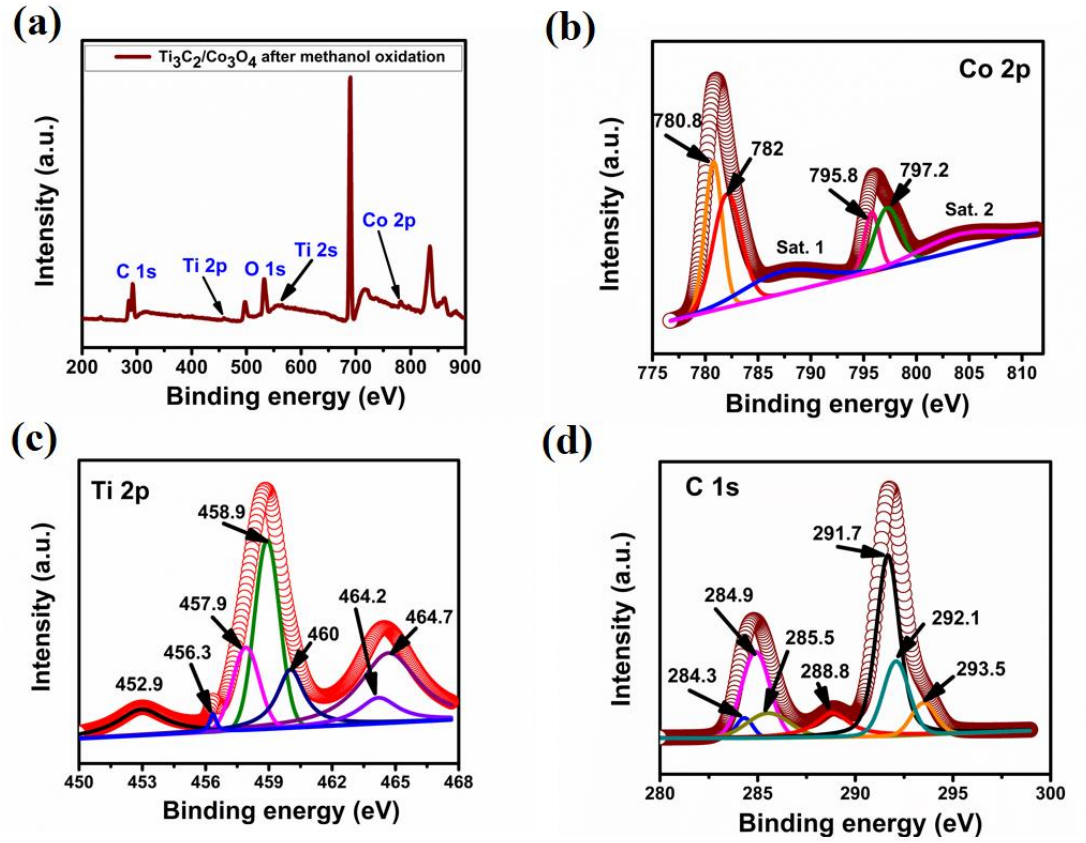

Figure 2.15: XPS of Ti_3C_2/Co_3O_4 after methanol oxidation: (a) Survey spectra, High-resolution XPS spectra of (b) Co 2p, (c) Ti 2p, and (d) C 1s

It is observed that the Co 2p peaks (fig. 2.15b) slightly shifts to higher binding energy values 780.8 (Co^{3+} $2p_{3/2}$), 782 (Co^{2+} $2p_{3/2}$), 795.8 (Co^{3+} $2p_{1/2}$), and 797.2 eV (Co^{2+} $2p_{1/2}$) after methanol oxidation. This increase in B.E. implies the release of electron from Co^{3+} and Co^{2+} ions. Moreover, the decrease in area of the peaks after methanol oxidation suggests the fact that Co ions are consumed in the electrochemical methanol oxidation

reaction. As can be seen from fig. 2.15c, the Ti 2p peaks are observed with slight changes in binding energy at 456.3, 457.9, 458.9, 460, 464.2, 464.7 eV corresponding to Ti $2p_{3/2}$-C, Ti $2p_{3/2}$-Ti $2p_{3/2}$, Ti $2p_{3/2}$-O, Ti $2p_{1/2}$-Ti $2p_{1/2}$, C-Ti($2p_{1/2}$)-T_x, Ti $2p_{1/2}$-O, respectively. The decrease in binding energy of Ti $2p_{3/2}$-Ti $2p_{3/2}$, Ti $2p_{1/2}$-Ti $2p_{1/2}$, and Ti $2p_{1/2}$-O occurs because of consumption of Ti in the electrochemical reactions. After continuous methanol oxidation a new peak emerges at 452.9 eV which corresponds to Ti-C interaction. The reduction in binding energy of Ti $2p_{3/2}$-C interaction and increase in Ti $2p_{3/2}$-O binding energy implies the formation of TiO_2. The high-resolution C 1s spectrum (displayed in fig. 2.15d) reveals 7 peaks on deconvolution. Peaks at 284.3, 284.9, 285.5, and 288.8 eV retain their binding energy; whereas, three additional peaks are observed at 291.7, 292.1, 293.5 eV which are due to the CHO compound mainly formaldehyde [67] and formate [68] formed as byproduct of methanol oxidation.

2.4 Conclusion

In conclusion, a mesoporous non-noble MOR electrocatalyst Ti_3C_2/Co_3O_4 is developed. As revealed by FESEM and TEM images, the nanocomposite Ti_3C_2/Co_3O_4 is composed of Co_3O_4 nanoparticles decorated over Ti_3C_2 MXene nanosheets. Mesoporous nature of the nanocomposite allows facile ion penetration into the catalyst leading to more electrode-electrolyte interactions. The nanocomposite Ti_3C_2/Co_3O_4 exhibits both surface and diffusion-controlled process with surface coverage of redox sites 1.9 times higher than Co_3O_4. The large surface area of MXene nanosheets, conducting network created by MXene nanosheets for Co_3O_4 nanoparticles and the strong interaction between MXene and Co_3O_4 are responsible for the enhanced surface coverage of redox sites, which leads to faster reaction kinetics of Ti_3C_2/Co_3O_4. Moreover, MXene nanosheets reduce aggregation of the Co_3O_4 nanoparticles, facilitating more and more charge transfer from Co_3O_4 to MXene nanosheets. The nanocomposite Ti_3C_2/Co_3O_4 offers high methanol oxidation current density of 38.38 A/g with low onset potential of 0.32 V at 20 mV/s. Lower Tafel slope (191 mV/dec) and lesser charge transfer resistance (7.45 Ω) of Ti_3C_2/Co_3O_4 /GC suggest its faster MOR kinetics. The existence of hydrophilic terminations in Ti_3C_2 MXene is confirmed by spectroscopic data. These terminations aid in the adsorption of more methanol molecules on the catalyst surface, enhancing MOR current. Moreover, these hydrophilic terminations recreate the active sites and increase the durability of the catalyst. Without experiencing significant catalyst surface

degradation, the catalyst remains stable up to 200 CV cycles. The MXene nanosheets get restacked and Co_3O_4 nanoparticles agglomerate after successive methanol oxidation for 200 cycles. The crystallinity also decreases due to degradation of the catalyst Ti_3C_2/Co_3O_4 over time. Few carbonate species and surface adsorbed methanol molecules can be confirmed from the FTIR spectra. The adsorbed formaldehyde formed as byproduct of methanol oxidation are confirmed from the XPS spectra. Thus, the nanocomposite is a promising methanol oxidation anode catalyst. However, if pure MXene devoid of any co-products could be composited with Co_3O_4, it can provide even better catalytic activity and be a potential candidate for energy storage and conversion applications.

2.5 References:

1. Jadhav, H. S., Roy, A., Chung, W. -J., Seo, J. G. Free standing growth of $MnCo_2O_4$ nanoflakes as an electrocatalyst for methanol electro-oxidation, *New J. Chem*., 41 (24):15058-15063, 2017.
2. Askari, M.B., Salarizadeh, P. and Beheshti-Marnani, A. A hierarchical hybrid of $ZnCo_2O_4$ and rGO as a significant electrocatalyst for methanol oxidation reaction: synthesis, characterization, and electrocatalytic performance. *Int J Energy Res*, 44 (11):8892-8903, 2020.
3. Tan, H.T., Sun, W., Wang, L. and Yan, Q. 2D transition metal oxides/hydroxides for energy-storage applications. *ChemNanoMat*, 2 (7):562-577, 2016.
4. Bhattacharya, K. and Deb, P. Hybrid nanostructured C-dot decorated Fe_3O_4 electrode materials for superior electrochemical energy storage performance. *Dalton Transactions*, 44 (19):9221-9229, 2015.
5. Baruah, K. and Deb, P. Electrochemically active site-rich nanocomposites of two-dimensional materials as anode catalysts for direct oxidation fuel cells: new age beyond graphene. *Nanoscale Advances*, 3 (13):3681-3707, 2021.
6. Mirzaeian, M., Akhanova, N., Gabdullin, M., Kalkozova, Z., Tulegenova, A., Nurbolat, S. and Abdullin, K. Improvement of the pseudocapacitive performance of cobalt oxide-based electrodes for electrochemical capacitors. *Energies*, 13 (19):5228, 2020.
7. Liu, J., Jiang, J., Cheng, C., Li, H., Zhang, J., Gong, H. and Fan, H.J. Co_3O_4 nanowire@ MnO_2 ultrathin nanosheet core/shell arrays: a new class of high-

performance pseudocapacitive materials. *Advanced Materials*, 23 (18):2076-2081, 2011.

8. Araújo, M.P., Nunes, M., Rocha, I.M., Pereira, M.F.R. and Freire, C. Co_3O_4 nanoparticles anchored on selectively oxidized graphene flakes as bifunctional electrocatalysts for oxygen reactions. *ChemistrySelect*, 3 (35):10064-10076, 2018.
9. Rajeshkhanna, G. and Rao, G.R. Micro and nano-architectures of Co_3O_4 on Ni foam for electro-oxidation of methanol. *Int. J. Hydrogen Energy*, 43 (9):4706-4715, 2018.
10. Liang, Y., Li, Y., Wang, H., Zhou, J., Wang, J., Regier, T. and Dai, H. Co_3O_4 nanocrystals on graphene as a synergistic catalyst for oxygen reduction reaction. *Nat Mater*, 10 (10):780-786, 2011.
11. Li, L., Zhou, G., Shan, X.Y., Pei, S., Li, F. and Cheng, H.M. Co_3O_4 mesoporous nanostructures@ graphene membrane as an integrated anode for long-life lithium-ion batteries. *J. Power Sources*, 255:52-58, 2014.
12. Cai, S., Wang, R., Yourey, W.M., Li, J., Zhang, H. and Tang, H. An efficient bifunctional electrocatalyst derived from layer-by-layer self-assembly of a three-dimensional porous Co-NC@ graphene. *Sci Bull*, 64 (14):968-975, 2019.
13. Shenashen, M.A., Hassen, D., El-Safty, S.A., Isago, H., Elmarakbi, A. and Yamaguchi, H. Axially oriented tubercle vein and X-crossed sheet of N-Co_3O_4@ C hierarchical mesoarchitectures as potential heterogeneous catalysts for methanol oxidation reaction. *Chem. Eng. J.*, 313:83-98, 2017.
14. Jun, B.M., Kim, S., Heo, J., Park, C.M., Her, N., Jang, M., Huang, Y., Han, J. and Yoon, Y. Review of MXenes as new nanomaterials for energy storage/delivery and selected environmental applications. *Nano Res*, 12:471-487, 2019.
15. Wang, K., Zhou, Y., Xu, W., Huang, D., Wang, Z. and Hong, M. Fabrication and thermal stability of two-dimensional carbide Ti_3C_2 nanosheets. *Ceram. Int.*, 42 (7):8419-8424, 2016.
16. Naguib, M., Kurtoglu, M., Presser, V., Lu, J., Niu, J., Heon, M., Hultman, L., Gogotsi, Y. and Barsoum, M.W. Two-dimensional nanocrystals produced by exfoliation of Ti_3AlC_2. *Adv. Mater*, 23 (37):4248-4253, 2011.
17. Seyedin, S., Yanza, E.R.S. and Razal, J.M. Knittable energy storing fiber with high volumetric performance made from predominantly MXene nanosheets. *J. Mater. Chem. A*, 5 (46):24076-24082, 2017.

18. Wen, M.Q., Xiong, T., Zang, Z.G., Wei, W., Tang, X.S. and Dong, F. Synthesis of MoS_2/gC_3N_4 nanocomposites with enhanced visible-light photocatalytic activity for the removal of nitric oxide (NO). *Opt. Express*, 24 (10):10205-10212, 2016.
19. Nan, J., Guo, X., Xiao, J., Li, X., Chen, W., Wu, W., Liu, H., Wang, Y., Wu, M. and Wang, G. Nanoengineering of 2D MXene-based materials for energy storage applications. *Small*, 17(9):1902085, 2021.
20. Abdullah, N., Saidur, R., Zainoodin, A.M. and Aslfattahi, N. Optimization of electrocatalyst performance of platinum–ruthenium induced with MXene by response surface methodology for clean energy application. *J. Cleaner Prod*, 277:123395, 2020.
21. Yang, X., Jia, Q., Duan, F., Hu, B., Wang, M., He, L., Song, Y. and Zhang, Z. Multiwall carbon nanotubes loaded with MoS_2 quantum dots and MXene quantum dots: Non–Pt bifunctional catalyst for the methanol oxidation and oxygen reduction reactions in alkaline solution. *Appl. Surf. Sci*., 464:78-87, 2019.
22. Lukatskaya, M.R., Mashtalir, O., Ren, C.E., Dall'Agnese, Y., Rozier, P., Taberna, P.L., Naguib, M., Simon, P., Barsoum, M.W. and Gogotsi, Y. Cation intercalation and high volumetric capacitance of two-dimensional titanium carbide. *Science*, 341 (6153):1502-1505, 2013.
23. Yu, X., Yin, W., Wang, T. and Zhang, Y. Decorating g-C_3N_4 nanosheets with Ti_3C_2 MXene nanoparticles for efficient oxygen reduction reaction. *Langmuir*, 35 (8):2909-2916, 2019.
24. Lu, Y., Fan, D., Chen, Z., Xiao, W., Cao, C. and Yang, X. Anchoring Co_3O_4 nanoparticles on MXene for efficient electrocatalytic oxygen evolution. *Science Bulletin*, 65 (6):460-466, 2020.
25. Roy, A., Jadhav, H.S., Thorat, G.M. and Seo, J.G. Electrochemical growth of $Co(OH)_2$ nanoflakes on Ni foam for methanol electro-oxidation. *New J. Chem*, 41 (17):9546-9553, 2017.
26. Tahir, M. Enhanced photocatalytic CO_2 reduction to fuels through bireforming of methane over structured 3D MAX Ti_3AlC_2/TiO_2 heterojunction in a monolith photoreactor. *Journal of CO_2 Utilization*, 38:99-112, 2020.
27. Alhabeb, M., Maleski, K., Anasori, B., Lelyukh, P., Clark, L., Sin, S. and Gogotsi, Y. Guidelines for synthesis and processing of two-dimensional titanium carbide ($Ti_3C_2T_x$ MXene). *Chem. Mater*, 29 (18):7633-7644, 2017.

28. Feng, A., Yu, Y., Jiang, F., Wang, Y., Mi, L., Yu, Y. and Song, L. Fabrication and thermal stability of NH_4HF_2-etched Ti_3C_2 MXene. Ceramics International, 43 (8):6322-6328, 2017.
29. Feng, A., Yu, Y., Wang, Y., Jiang, F., Yu, Y., Mi, L. and Song, L. Two-dimensional MXene Ti_3C_2 produced by exfoliation of Ti_3AlC_2. *Materials & Design*, 114:161-166, 2017.
30. Cai, T., Wang, L., Liu, Y., Zhang, S., Dong, W., Chen, H., Yi, X., Yuan, J., Xia, X., Liu, C. and Luo, S. Ag_3PO_4/Ti_3C_2 MXene interface materials as a Schottky catalyst with enhanced photocatalytic activities and anti-photocorrosion performance. *Applied Catalysis B: Environmental*, 239;545-554, 2018.
31. Hu, Z., Kuai, X., Chen, J., Sun, P., Zhang, Q., Wu, H.H. and Zhang, L. Strongly coupled MoS_2 nanocrystal/Ti_3C_2 nanosheet hybrids enable high-capacity lithium-ion storage. *ChemSusChem*, 13 (6):1485-1490, 2019.
32. Khanam, R. and Mohanta, D. Properties of hydrothermally processed multi-walled titania nanotubes. Physica E: Low-dimensional Systems and Nanostructures, 49:39-43, 2013.
33. Qasem, M.A.A., Khan, A., Onaizi, S.A., Mohamed, H.D., Helal, A. and Aziz, M.A. Effect of $Co(NO_3)_2 \cdot 6H_2O$ thermal decomposition temperature on the nano-Co_3O_4 product morphology and electrocatalysis of water oxidation. , *J. Appl. Electrochem.*, 49:251-259, 2019.
34. Tahir, M. Construction of a stable two-dimensional MAX supported protonated graphitic carbon nitride (pg-C_3N_4)/Ti_3AlC_2/TiO_2 Z-scheme multiheterojunction system for efficient photocatalytic CO_2 reduction through dry reforming of methanol. *Energy Fuels*, 34 (3):3540-3556, 2020.
35. Xu, C., Yang, F., Deng, B., Zhuang, Y., Li, D., Liu, B., Yang, W. and Li, Y., Ti_3C_2/TiO_2 nanowires with excellent photocatalytic performance for selective oxidation of aromatic alcohols to aldehydes. *J. Catal.*, 383:1-12, 2020.
36. Liu, N., Lu, N., Yu, H., Chen, S. and Quan, X. Efficient day-night photocatalysis performance of 2D/2D Ti_3C_2/Porous g-C_3N_4 nanolayers composite and its application in the degradation of organic pollutants. *Chemosphere*, 246:125760, 2020.
37. Xu, H., Hai, Z., Diwu, J., Zhang, Q., Gao, L., Cui, D., Zang, J., Liu, J. and Xue, C. Synthesis and microwave absorption properties of core-shell structured Co_3O_4-PANI nanocomposites. *J. Nanomater.*, 2015:9-9, 2015.

38. Nazir, R., Khalfani, A., Abdelfattah, O., Kumar, A., Saleh Saad, M.A. and Ali, S. Nanosheet synthesis of mixed Co_3O_4/CuO via combustion method for methanol oxidation and carbon dioxide reduction. *Langmuir*, 36 (42):12760-12771, 2020.
39. Ahmed, B., Anjum, D.H., Hedhili, M.N., Gogotsi, Y. and Alshareef, H.N. H_2O_2 assisted room temperature oxidation of Ti_2C MXene for Li-ion battery anodes. *Nanoscale*, 8 (14):7580-7587, 2016.
40. Yang, C., Jiang, Q., Huang, H., He, H., Yang, L. and Li, W. Polyelectrolyte-Induced Stereoassembly of Grain Boundary-Enriched Platinum Nanoworms on $Ti_3C_2T_x$ MXene Nanosheets for Efficient Methanol Oxidation. ACS Appl. Mater. Interfaces, 12 (21):23822-23830, 2020.
41. Ashok, A., Kumar, A., Ponraj, J., Mansour, S.A. and Tarlochan, F. Single step synthesis of porous $NiCoO_2$ for effective electrooxidation of glycerol in alkaline medium. *J. Electrochem. Soc*., 165 (15):J3301-J3309, 2018.
42. Elgrishi, N., Rountree, K.J., McCarthy, B.D., Rountree, E.S., Eisenhart, T.T. and Dempsey, J.L. A practical beginner's guide to cyclic voltammetry. *J. Chem. Educ.*, 95 (2):197-206, 2018.
43. Farida, A.N., Fitriany, E., Baktir, A., Kurniawan, F. and Harsini, M. Voltammetric study of ascorbic acid using polymelamine/gold nanoparticle modified carbon paste electrode. *IOP Conf. Ser.: Earth Environ. Sci.*, 217 (1):012004, 2019.
44. Danaee, I., Jafarian, M., Mirzapoor, A., Gobal, F. and Mahjani, M.G. Electrooxidation of methanol on NiMn alloy modified graphite electrode. *Electrochim. Acta*, 55 (6):2093-2100, 2010.
45. Majdi, S., Jabbari, A., Heli, H. and Moosavi-Movahedi, A.A. Electrocatalytic oxidation of some amino acids on a nickel–curcumin complex modified glassy carbon electrode. *Electrochim. Acta*, 52 (14):4622-4629, 2007.
46. Wang, W., Li, R., Zhang, R., Ma, J., Wang, B. *J. Electroanal. Chem*., 2015, **742**, 110-121.
47. Wang, W., Li, R., Zhang, R., Ma, J. and Wang, B., 2015. Electrocatalytic oxidation of methanol on glassy carbon electrode modified with nickel–manganese salen complexes encapsulated in mesoporous zeolite A. *J. Electroanal. Chem*., 742:110-121, 2015.

48. Alotaibi, N., Hammud, H.H., Al Otaibi, N. and Prakasam, T. Electrocatalytic properties of 3D hierarchical graphitic carbon–cobalt nanoparticles for urea oxidation. *ACS omega*, 5 (40):26038-26048, 2020.
49. Xu, H., Shen, K., Liu, S., Zhang, L.C., Wang, X., Qin, J. and Wang, W. Micromorphology and phase composition manipulation of nanoporous gold with high methanol electro-oxidation catalytic activity through adding a magnetic field in the dealloying process. *J. Phys. Chem. C*, 122 (6):3371-3385, 2018.
50. Baruah, B. and Kumar, A., 2018. PEDOT: PSS/MnO_2/rGO ternary nanocomposite based anode catalyst for enhanced electrocatalytic activity of methanol oxidation for direct methanol fuel cell. *Synthetic Metals*, 245:74-86, 2018.
51. Lang, Z., Zhuang, Z., Li, S., Xia, L., Zhao, Y., Zhao, Y., Han, C. and Zhou, L. MXene surface terminations enable strong metal–support interactions for efficient methanol oxidation on palladium. *ACS Appl. Mater. Interfaces*, 12 (2):2400-2406, 2020.
52. Yang, C., He, H., Jiang, Q., Liu, X., Shah, S.P., Huang, H. and Li, W. Pd nanocrystals grown on MXene and reduced graphene oxide co-constructed three-dimensional nanoarchitectures for efficient formic acid oxidation reaction. *Int. J. Hydrogen Energy*, 46 (1):589-598, 2021.
53. Wang, Y., Wang, J., Han, G., Du, C., Deng, Q., Gao, Y., Yin, G. and Song, Y. Pt decorated Ti_3C_2 MXene for enhanced methanol oxidation reaction. *Ceram. Int.*, 45 (2):2411-2417, 2018.
54. Lewalska-Graczyk, A., Pieta, P., Garbarino, G., Busca, G., Holdynski, M., Kalisz, G., Sroka-Bartnicka, A., Nowakowski, R., Naushad, M., Gawande, M.B. and Zboril, R. Graphitic carbon nitride–nickel catalyst: from material characterization to efficient ethanol electrooxidation. *ACS Sustainable Chem. Eng.*, 8 (18):7244-7255, 2020.
55. Gao, Z., Li, M., Wang, J., Zhu, J., Zhao, X., Huang, H., Zhang, J., Wu, Y., Fu, Y. and Wang, X. Pt nanocrystals grown on three-dimensional architectures made from graphene and MoS_2 nanosheets: highly efficient multifunctional electrocatalysts toward hydrogen evolution and methanol oxidation reactions. *Carbon*, 139:369-377, 2018.
56. Zhai, C., Zhu, M., Bin, D., Ren, F., Wang, C., Yang, P. and Du, Y. Two dimensional MoS_2/graphene composites as promising supports for Pt electrocatalysts towards methanol oxidation. *J. Power Sources*, 275:483-488, 2015.

57. Kannan, R., Kim, A.R., Nahm, K.S., Lee, H.K. and Yoo, D.J. Synchronized synthesis of Pd@C-RGO carbocatalyst for improved anode and cathode performance for direct ethylene glycol fuel cell. *Chem. Commun.*, 50 (93):14623-14626, 2014.
58. Kannan, R., Lim, C.D., Kim, A.R., Lee, M.H. and Yoo, D.J. Bifunctional Electrocatalyst of Pd-C@MoS_2-RGO Hybrid Nanostructures—Size Confined Green Synthesis for Direct Alcohol Fuel Cells. *J. Nanosci. Nanotechnol*., 19 (8):4520-4528, 2019.
59. Wang, H.D., Wang, X.F., Su, F., Li, J.S., Zhang, L.C., Sang, X.J. and Zhu, Z.M. Carboxyethyltin and transition metal co-functionalized tungstoantimonates composited with polypyrrole for enhanced electrocatalytic methanol oxidation. *Dalton Trans*., 48 (9):2977-2987, 2019.
60. Raoof, J.B., Ojani, R. and Hosseini, S.R. An electrochemical investigation of methanol oxidation on nickel hydroxide nanoparticles. *S. Afr. J. Chem*., 66:47-53, 2013.
61. Khalafallah, D., Alothman, O.Y., Fouad, H. and Khalil, K.A., 2018. Hierarchical Co_3O_4 decorated PPy nanocasting core-shell nanospheres as a high performance electrocatalysts for methanol oxidation. *Int. J. Hydrogen Energy*, 43 (5):2742-2753, 2018.
62. Sandoval-González, A., Borja-Arco, E., Escalante, J., Jiménez-Sandoval, O. and Gamboa, S.A. Methanol oxidation reaction on $PtSnO_2$ obtained by microwave-assisted chemical reduction. *Int. J. Hydrogen Energy*, 37 (2):1752-1759, 2012.
63. Suen, N.T., Hung, S.F., Quan, Q., Zhang, N., Xu, Y.J. and Chen, H.M., Electrocatalysis for the oxygen evolution reaction: recent development and future perspectives. *Chem. Soc. Rev*., 46(2):337-365, 2017.
64. Galal, A., Atta, N.F. and Hefnawy, M.A. Lanthanum nickel oxide nano-perovskite decorated carbon nanotubes/poly (aniline) composite for effective electrochemical oxidation of urea. *J. Electroanal. Chem.*, 862:114009, 2020.
65. Wang, P., Cui, H. and Wang, C. In situ formation of porous trimetallic PtRhFe nanospheres decorated on ultrathin MXene nanosheets as highly efficient catalysts for ethanol oxidation. *Nano Energy*, 66:104196, 2019.
66. Manzoli, M., Vindigni, F., Tabakova, T., Lamberti, C., Dimitrov, D., Ivanov, K. and Agostini, G. Structure–reactivity relationship in Co_3O_4 promoted Au/CeO_2 catalysts

for the CH_3OH oxidation reaction revealed by in situ FTIR and operando EXAFS studies. *J. Mater. Chem. A*, 5 (5):2083-2094, 2017.

67. Kawashima, A., Asami, K. and Hashimoto, K. XPS analysis of amorphous Ni Nb Sn Pt alloy catalysts for electro-oxidation of formaldehyde. *Mater. Sci. Eng. A*, 134:1070-1073, 1991.
68. Vohs, J.M. and Barteau, M.A. Conversion of methanol, formaldehyde and formic acid on the polar faces of zinc oxide. *Surface science*, 176 (1-2):91-114, 1986.